# Improving the performance of horizontal axial wind turbines using Bio-inspired airfoil shapes for its blades at low Reynolds numbers

**By**

**Tshamano Nemirini**

*A Dissertation research report submitted to fulfil the requirements of Magister Technologiae in Engineering*

*&*

*at the*

*University of South Africa*

**Department of Electrical and Mining Engineering, University of South Africa,**
**Private Bag X6, FLORIDA, 1710, SA,**

*Supervisor: Dr Wei Hua Ho*

*Final Academic year: 31 January 2021*

## Declaration 1 - Plagiarism

Name: Tshamano Nemirini

Student Number: 44063873

Degree: **Magister Technologiae**

**Degree Code: DFEEN91**

# Improving the performance of horizontal axial wind turbines using Bio-inspired airfoil shapes for its blades at low Reynolds numbers

I declare that the above dissertation is my work and that all the sources that I have used or quoted have been indicated and acknowledged by means of complete references.

I further declare that I submitted the dissertation to originality checking software and that it falls within the accepted requirements for originality.

I further declare that I have not previously submitted this work, or part of it, for examination at Unisa for another qualification or at any other higher education institution.

Signed: ____________________ Date: 31 January 2021

## Abstract

Small-scale wind turbines were not considered viable in the past due to their poor efficiencies, mainly because of their aerodynamic effects around the irfoil shape. Recently researchers have renewed interest in enhancing the aerodynamic performances of the blades' designs inspired by the aerodynamic pattern of biological characteristics of insects and marine mammals such as locusts, dragonflies, damselflies, Humpback Whales etc. Bio-inspired wing designs have advantages compared to conventional smooth irfoil blades as they can counter the bending forces that the wings experience during flapping.

Bio-inspired corrugated airfoil based on dragonfly wing geometries have been reported to perform well compared to conventional airfoil at low Reynolds numbers. Corrugated airfoils reduce flow separation and enhance aerodynamic performance by trapping vortices in the corrugations thus drawing flow towards the airfoil's surface. This results in the higher lift whilst incurring only marginally higher drag. Such airfoils also have an advantage when it comes to span-wise structural stiffness due to the corrugated cross-sections.

Replacing conventional turbine blades by tubercles or corrugated blades could enhance turbine performance by reducing the pressure gradient along the leading edge; however, the aerodynamic effects at the leading edge will depend on the variations of wavelength and amplitude.

In this study, two types of computational studies were investigated: Optimising a corrugated airfoil and investigating the aerodynamic effects of a sinusoidal shape at the leading edge of a blade.

Previous studies used an idealized geometry based on the dragonfly wing cross-section profile but did not attempt to optimize the geometry. In the present study: a two-dimensional CFD model is constructed using ANSYS Fluent Workbench-Design Explorer to determine the optimal corrugated blade profile for four angles of attack (AOA) from 5° to 20° corresponding to typical AOA of small-scale wind turbine blades.

Two modified blades with variations of wavelength and amplitude at the leading edge were studied to investigate the aerodynamic effects. Three-dimensional models were constructed using Qblade software and 3D points were exported to AutoCAD Inventor to generate the CAD model. The governing equations used are continuity and Navier-Stokes equations written in a frame reference rotating with the blade. The CFD package used is ANSYS

FLUENT 19.0. The simulation was run under steady-state, using SST-k omega turbulence model.

The modifications have improved the aerodynamic performance. The optimised corrugated blade produced a maximum increase of $C_L$ and L/D.

Both modified blades (1 and 2) had their performances measured separately and compared to that of baseline blade SG6042 (Conventional blade). Modified blade 1 had a lower wavelength and amplitude at the leading edge of 14.3 % and 4 % respectively of the chord. It was noted that the aerodynamic performance decreased by 6%. Modified model 2, on the other hand had a higher wavelength and amplitude at the leading edge. of 40.4 % and 11.9 % respectively of the chord. It was also noted the aerodynamic performance increased by 6%. From the empirical evidence highlighted above, it can be observed that there is a direct correlation between wavelength, amplitude, and aerodynamic performance of the blade.

**Keywords:** Corrugated airfoil, leading-edge tubercles, Humpback whale fins, dragonfly wing, Low Reynolds Number, Small-scale Horizontal wind turbines, Geometry Shape optimization.

## Acknowledgements

My studies with the University of South Africa (UNISA) would not have been possible without the guidance and support from family, friends, supervisors, and organizations of Computational Fluids Dynamics.

I want to give special thanks to my father and my late mother for understanding and to give me a chance to further my studies. Even though our family is going through financial strains, this means a lot to me, and I acknowledge that they sacrificed to further my studies.

Finally, I gratefully acknowledge that this research work was funded by The National Research Foundation (NRF) of South Africa and The Science and Technology Development Fund (STDF) of Egypt and I am thankful to carry out this research and to be a team member of South-Egypt joint Researchers.

# Table of Contents

## List of Figures

## List of Tables

**Nomenclature**

| Symbol | Name | Units |
|---|---|---|
| | | |
| Cp | Coefficient of Power | Dimensionless |
| $C_L$ | Coefficient of Lift Force | Dimensionless |
| $C_d$ | Coefficient of Drag Force | Dimensionless |
| FL | Lift Force | N |
| FD | Drag force | N |
| $C_m$ | Coefficient of Moment | Dimensionless |
| Kn | Knudsen Number | Dimensionless |
| $\tau$ | Moment | $Kgm^2/s^2$ |
| T | Temperature | °C |
| C | Chord Length | M |
| $\rho$ | Density | $Kg/m^3$ |
| A | Swept area of blades | $m^2$ |
| V | Wind speed | m/s |
| V | Volume | $m^3$ |
| Re | Reynolds number | Dimensionless |
| a | Speed of sound | 343 m/s |
| P | Pressure | Pa |
| P | Power | Kw |
| M | Mach Number | Dimensionless |
| L | Length | m |
| L | Characteristic length of flow field | m |
| $\lambda$ | Mean Free Path Length | m |
| Ø | Angle of Attack | ° |
| $\mu$ | Dynamic Viscosity | $N.S/m^2$ |
| ט | Kinematic Viscosity | Kg/ms |
| t | Thickness | m |
| N | Molecules | 1 mole = $6.02x\ 10^{23}$ |
| r | Particle molecule radius | m |
| n | Number of Moles | mol |
| $R_u$ | Specific Gas Constant | $8.31447\ \frac{KJ}{K}.mol.K$ |
| P | Atmospheric Pressure | Pa |
| Z | Centre of Pressure | m |
| $\gamma$ | Specific heat ratio | Dimensionless |
| | | |

## List of Acronyms

| | |
|---|---|
| **HAWT** | Horizontal axis Wind Turbine |
| **VAWT** | Vertical-axis Wind Turbine |
| **2D** | Two Dimensional |
| **3D** | Three Dimensional |
| **CFD** | Computational Fluid Dynamics |
| **HPC** | High-Performance Computers |
| **NS** | Navier stokes |
| **Re** | Reynolds Number |
| **RET** | Renewable energy technology |
| **EIA** | Energy Information Administration |
| **IRP** | Integrated Resource Plan |
| **MW** | MegaWatts |
| **RES** | Renewable Energy Sources |
| **SA** | South Africa |
| **AOA** | Angle of Attack |
| **NACA** | National Advisory Committee for Aeronautics |
| **KW** | Kilowatts |
| **NREL** | National Renewable Energy Laboratory |
| **AR** | Aspect Ratio |
| **DOE** | Design of Experiments |
| **CCD** | Central Composite Design |
| **CAD** | Computer-Aided Design |
| **MRF** | Moving Reference Frame |
| **AFC** | Active Flow Control |

| | |
|---|---|
| **PIV** | Particle image velocimetry |
| **RPM** | Revolutions per minute |
| **KW h** | Kilowatt-hour |

# 1. INTRODUCTION

## 1.1 Renewable Energy

Energy is an essential part of human life. It is used to heat homes, fuel transportation and generate electricity. A high percentage of this energy is normally generated from fossil fuels e.g., oil, coal, and gas [1]. Looking at the growth of industries in developing and developed countries as well as the rapid population increase, the swift increase in energy consumption is apparent, which raises concerns regarding the diminishing fossil fuel reserves and the greenhouse effect of burning these fossil fuels [2]. The pie chart below depicts the primary energy sources in South Africa, it can be seen that renewable energy takes up 11 % of energy consumption with coal taking up 69% and oil 11%.

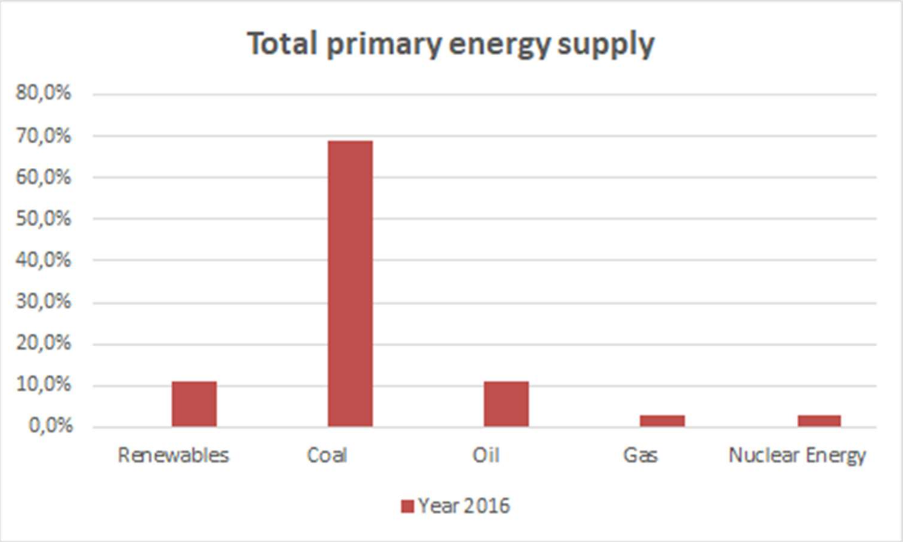

*Figure 1: Energy Consumption in South Africa, 2011 [2]*

There is a need to find alternative sources of energy to meet the skyrocketing energy demands for modern services and there is a need to reduce the emission of greenhouse gases. This has led to research and investment in renewable energy technology (RET). Harnessing renewable energy requires a thorough understanding of energy cycles, given below is a brief description. The sun supplies the earth with a vast amount of energy (light and heat). The majority of this energy is absorbed by the environment and transformed into different renewable energy flows such as wind and biomass energy. By using alternative technologies this energy can be utilized to generate renewable energy flows e.g., solar, biogas and wind. Renewable energy flows can reduce greenhouse gas emission by replacing coal as our main energy source [3]. Using renewable energy presents many advantages, such as reducing the cost of raw material and using locally accessible resources which will create employment opportunities [4].

The world is facing financial instability of energy cost, this is because fossil energy is non-renewable and the expectation of energy demand has increased rapidly [5] throughout the years as depicted in Figure 2.

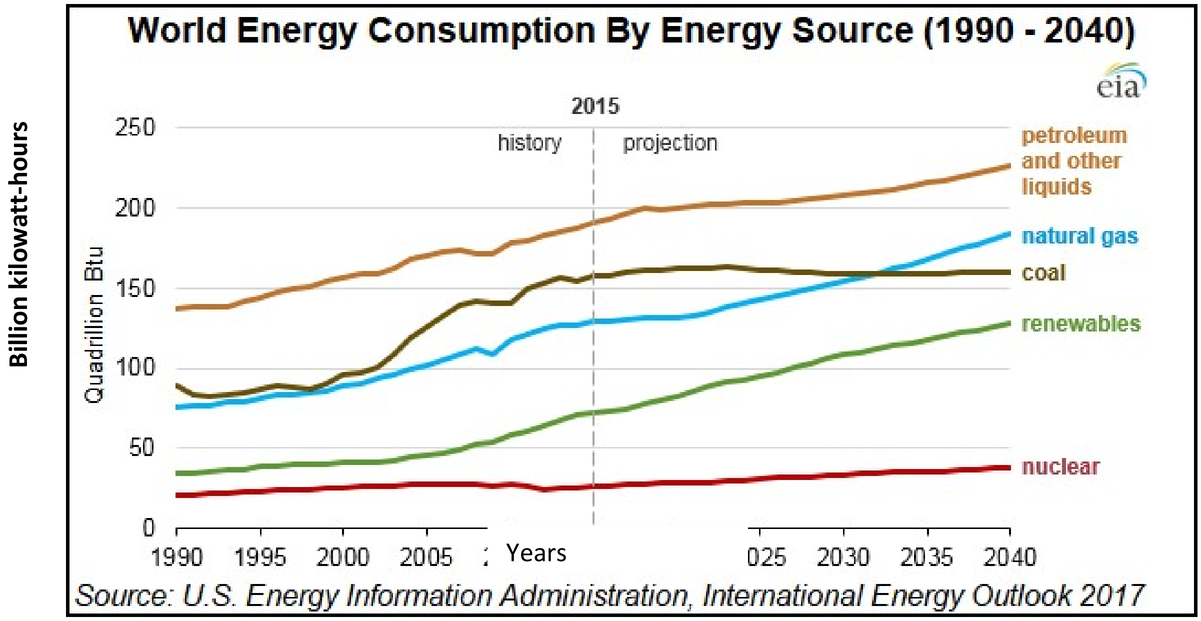

Source: U.S. Energy Information Administration, International Energy Outlook 2017

***Figure 2: World Energy consumption [5]***

The Energy Information Administration (EIA) has shown that the average cost of fuel throughout the world has varied considerably in the past few decades and there is a consistent upward trend in the price for crude oil. As shown in Figure 2, electricity generation from renewable sources is projected to be constant whereas fossil fuel is projected to increase the projections of future energy demands. it is clear from Figure 2 that alternative energy must be implemented around the world, and it must be a primary energy source to promote climate protection.

Currently, non-renewable energy is driven by the demand for electricity, not environmental concerns. Fossil fuel normally emits a substantial concentration of toxic, greenhouse gases during combustion. Future developments have focused on wind and other renewable energy sources since they can meet the demand without a negative environmental impact [5].

It is clear that there is a need for improving renewable energy to limit climate pollution from fossil fuel and an economical advantage will result.

Literature has shown that energy demands have spiked in recent years and projections show a bigger demand in the near future due to the development of advanced technology. Energy is in high demand in developing countries or dense populations. International Energy Agency (IEA) statistics show that energy demand increases by 2% annually [5]. Although fossil energy is taken as primary energy to meet the global demand, it is well understood that it has a major impact: The environmental consequences of burning fossil fuel are air, soil, and water contamination and more.

Renewable energy exploration in South Africa has improved and developed significantly while stimulating projects that utilize alternative energy sources. Renewable energy is becoming a growing market in SA and it would be advantageous to devote our resources to alternative sources of energy for powering organisations and households. Eskom is presently constructing two 4800 MW coal-fired power stations in Limpopo province, and Mpumalanga province. Despite these coal-fired power stations construction, the country still has energy shortages resulting in load shedding and adversely affecting the efficient operation of other institutions [6, 7].

Photovoltaic and wind energy are some of the most abundant renewable energy sources (RES) in South Africa, the country being among the top 3 in the globe when it comes to the number of direct sunshine hours annually [2]. Additional commercially active RES projects in SA comprise biogas & biomass, concentrated solar, solar water heating technologies and hydroelectricity. South Africa currently does not have any plants for wave energy, this technology is still in its research stage. A recently commissioned wind farm located in Eastern Cape (Nxuba wind Farm) can produce 1.26Gwh/year to feed into the national grid. This shows that South Africa is investing in renewable energy [8].

## 1.2 Wind Turbines background

Wind energy has been in use for centuries as a natural source of energy, it has been in use to accomplish many tasks, such as pumping water (e.g., Windmill), propelling ships, and processing grains and partly to generate electricity. Modern versions of windmills are known as wind turbines. Wind turbines are described as machines that can convert kinetic energy into electrical energy. In present day wind turbines, the aerodynamic force acting on the rotating shaft is used to produce a net momentum, this is how mechanical power is produced which is then converted into electrical energy by a generator [9].

Two main types of wind turbines are commonly used: a horizontal axis wind turbine (HAWT) and a vertical axis wind turbine (VAWT). The common variance amongst the main types of turbines is the orientation; Blades may be arranged either in a vertical or horizontal configuration as shown in Figure 3.

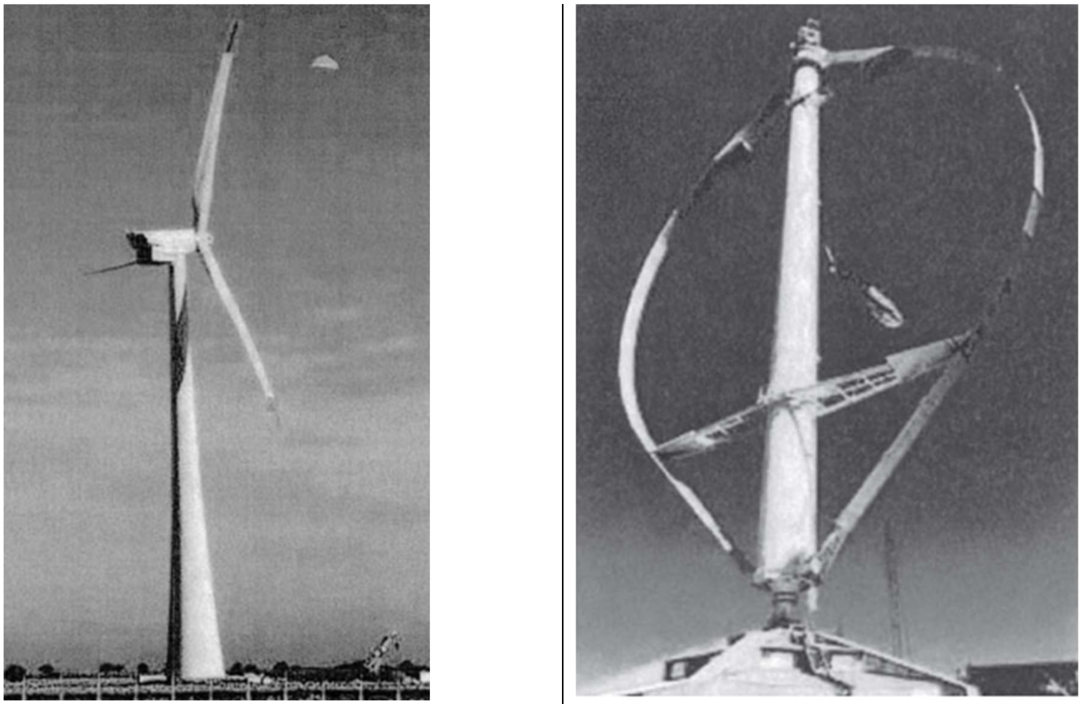

(a) Horizontal Axis (b) Vertical Axis

*Figure 3: Typical common types of Wind Turbines [11]*

Furthermore, wind turbines system can either be a drag or lift system. Drag systems are wind turbines that apply pressure on the body in the flow direction, while lift systems are wind turbines that apply force perpendicular to the relative flow. The lift system is preferred as it results in a higher force per area [11]. Horizontal and vertical axis wind turbines have their advantages and disadvantages. Below in Table 1 is a comparison of HAWT and VAWT systems.

**Table 1: Comparison between HAWT and VAWT Turbines**

| Item | Category | Comparison |
|---|---|---|

| | | Horizontal axis wind turbine (HAWT) | Vertical axis wind turbine (VAWT) |
|---|---|---|---|
| 1 | Capital Cost | the initial expenditure on HAWT systems is much higher than VAWT | Transmission losses are reduced (cost-efficient). |
| 2 | Plant Maintenance | Not easily accessible for maintenance | The location of the system is near ground level, and this makes it easier to access maintenance |
| 3 | Power Outputs | They are generally designed to generate electricity from high wind speed, | They are generally designed to generate electricity from low wind speed,<br>No need for a yaw mechanism, as they can catch the wind in all directions, this is important as it simplifies the design stage by not including a yaw mechanism,<br>Power output may be affected in gust wind areas. |
| 4 | Noise | Too Noisy | Noise level meets atmospheric requirements |
| 5 | Plant lifetime | HAWT turbines have a long life span. | VAWT turbines have a short life span, their turbine blades are vulnerable to fatigue because of applied force with every rotation (Cyclic loading). |
| 6 | Power coefficient | High efficiency, up to 50% at the speed ratio greater than 6 | Low efficiency, up to 40% at the speed ratio greater than 5 |

As shown in Table 1, both VAWT and HAWT are used to generate electrical power, each depending on its application.

Harnessing electricity from wind was not in favour due to several reasons: Global energy requirements are met and supplied primarily by fossil fuel (Coal, Natural Gas & Oil) [1, 10]. The low efficiency of wind turbines could not meet global requirements, and they were not fully reliable as the wind varies based on their geographical regions and time of the year.

Most developments of wind turbines in the last few decades focused more on larger systems; small-scale wind turbines were not considered due to low efficiencies [11]. The main reasons for the low efficiencies of small-scale systems are due to the poor performance of conventional smooth airfoil blades at low Reynolds numbers. The aerodynamic characteristics of insects and marine mammals such as locusts, dragonflies, damselflies, Humpback Whales etc. have been reported to perform better compared to conventional airfoils at low Reynolds numbers. Replacing conventional turbine blades by Bio-inspired blades is predicted to enhance turbine performance.

For this study, HAWT has been chosen because it produces maximum performance compared to all other types of wind turbines, with approximately 60% efficiency [12].

## 1.3 Two-Dimensional Aerodynamics

For simplicity, the flow at a given radial position of the wind turbine wingspan, forces can be analysed in two dimensions. The resultant force from the flow depends on the x and y-axis velocity components whereas the z-axis velocity component is taken as 0 m/s. The turbine aerodynamic power output can then be expressed by the following equation,

$$P = \frac{1}{2} C_p \rho A V^3 \tag{1.3.1}$$

Where,

P = Output power [Kw]

Cp = Coefficient of power

$\rho$ =Density [kg/m$^3$]

A = Swept area of blades [m$^2$]

V = Wind Speed [m/s]

As shown on the force vector triangle below in Figure 4, the relative wind approaches the wing at an angle of attack, this, however, creates resulting force from a component of lift force and drag force. One of the main goals in wind engineering designs is to minimise drag force and to increase lift force. The aerodynamic performance of a wind turbine depends on the ratio of maximum Lift force over Drag force and the torque produced by the blades. The Lift and Drag force equations are expressed as follows,

$$FL = \frac{1}{2} C_l \rho V^2 A \tag{1.3.2}$$

$$FD = \frac{1}{2} C_d \rho V^2 A \tag{1.3.3}$$

Where,

FL = Lift Force [N]

FD = Drag Force [N]

$C_d$ = Coefficient of Drag

$C_L$ = Coefficient of Lift

$\rho$= Density [kg/m$^3$]

A = Swept area of blades [m$^2$]

$V_w$ = Wind Speed [m/s]

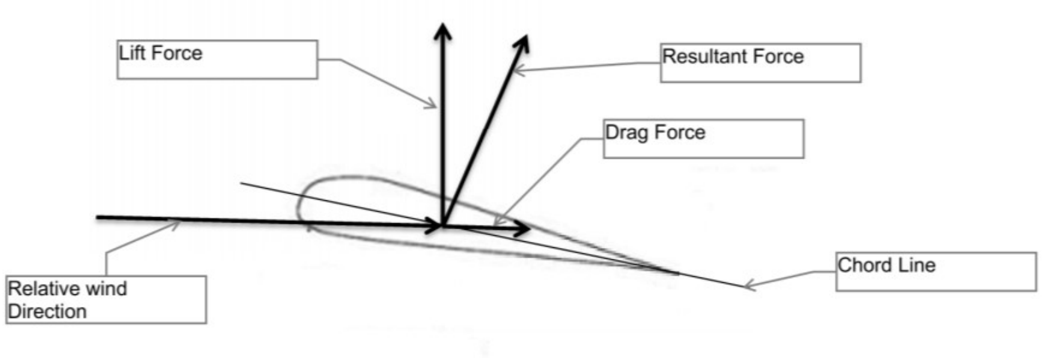

*Figure 4: Force Vector Triangle on an airfoil [10]*

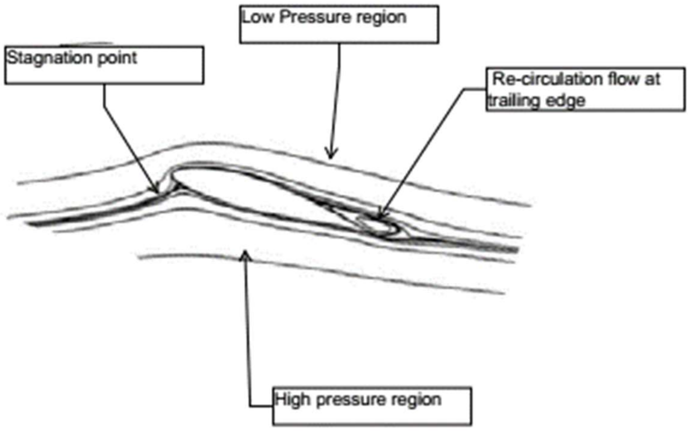

*Figure 5: Schematic view of streamline past an airfoil [10]*

As illustrated in Figure 5, the moment also contributes to generating a lift force. The airfoil has a low-pressure region on the top area/surface and a high-pressure region at the bottom area/surface.

## 1.4 Bio-Inspired airfoil shapes

The engineers and biologist have focused on improving the engineering systems by mimicking bionic study. The attempt to adapt nature's solution to physical challenges towards solving engineering problems is that nature is well-honed. Electricity generation from renewable sources is regarded as future-proof as its advantages were indicated in section 1.1.

Small-scale horizontal axial wind turbines were not considered due to their poor aerodynamic performances; however, this research has been revisited lately looking closely at how nature has overcome this challenge i.e., instead of looking at conventional airplane airfoils derived from birds wings, we should consider looking at the cross-sectional profiles of insects such as dragonflies and bumblebees are corrugated or cross-sectional profiles of humpback whale flippers have tubercles at the leading edge. The bionic effects of this research will be covered in detail in the literature review section.

## 1.5 Motivation

Small-scale wind turbines can be grid-connected systems or off-grid systems. In most geographic areas where wind speed is ±3m/s, small-scale wind turbines are not applicable due to their poor efficiency. The focus of the research is to improve the performance of small-scale horizontal axial wind turbine by means of bio-inspired airfoil shapes for its blades at low Reynolds numbers Re= 34, 000 – 250 000 so that sustainable energy will be obtained.

The motivation of the research is inspired by the aerodynamic pattern of biological characteristics of insects and marine mammals such as locusts, dragonflies, damselflies, Humpback Whales, etc.

Bio-inspired corrugated airfoils based on dragonfly wing geometries or Humpback whale fin on the leading-edge of the wing as shown in Figure 6 have been reported to perform well compared to conventional airfoils at low Reynolds numbers. Corrugated airfoil reduces flow separation and enhances aerodynamic performance by trapping vortices in the corrugations thus drawing flow towards the airfoil surface. This results in the higher lift whilst incurring only marginally higher drag [23 - 30]. Such airfoils also have an advantage when it comes to span-wise structural stiffness due to the corrugated cross-sections.

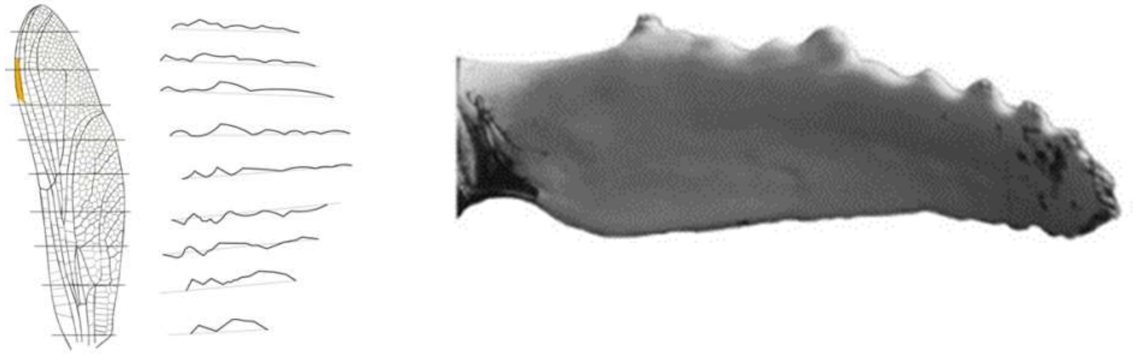

(a). Typical Dragonfly wing Corrugations along the span

(b). Typical Humpback Whale Wing with Tubercles at the leading edge *[37]*

*Figure 6: Typical Dragonfly wing and Humpback Whale Wing*

On the other hand, the leading edge of a humpback whale wing has tubercles that function as passive-flow control features which in turn enhance the performance of the flipper. This results in creating counter-rotating vortices that delay stall [36- 39].

Modifying conventional turbine blades with tubercles at the leading edge could enhance turbine performance by reducing the pressure gradient along the leading edge, however, the aerodynamic effects at the leading edge will depend on the variations of wavelength [1] and amplitude [2] of sinusoidal shape.

---

[1] The distance between successive crests of a rounded tubercles,

[2] The maximum distance between crest or trough to origin position.

## 1.6 Potential Benefits

The section below focuses on potential areas that are suitable for locating small horizontal wind turbines. Small-scale wind turbines are exposed to external environmental impacts that may affect their functionality. Appropriate safety and reliability must be considered in the design stage. The most common environmental condition that affects the structural integrity in wind turbines is wind conditions.

Normal external environmental conditions for small-scale wind turbines have benefits in long fatigue life, while extreme conditions will result in a short fatigue life. These environmental conditions depend on the intended site or suitable areas where the wind turbines are installed. Wind speed values are intended to represent the characteristic values of many different sites, although this is not an accurate representation of a specific site.

Wind energy resources in South Africa are influenced by the regions' weather fluctuations that are different between the summer and winter season [13]. In the summer, wind movements are concentrated in the south of the continent, this is mainly caused by the Atlantic Oceans westerly winds. In winter, wind movement is concentrated in the north of the continent, the strong winds are usually caused by cold fronts moving from the southern part of South Africa.

Strong winds in South Africa are mainly caused by thunderstorms and wave cyclones of low pressure. Figure 7depicts the zones identifying locations where strong winds are likely to dominate in South Africa [13]. Intense thunderstorms, tornados and downpours normally occur at some part of climatic Zone 2 and Zone 5 (Temperate interior and Sub-Tropical Costal), frequently occurs during summer seasons. Southern and western part climatic Zone 4 (Temperate Coastal) are not much affected. The total area affected for Zone 2 and Zone 5 is approximately 225 000 km$^2$ and 60 000km$^2$ for Zone 4[13].

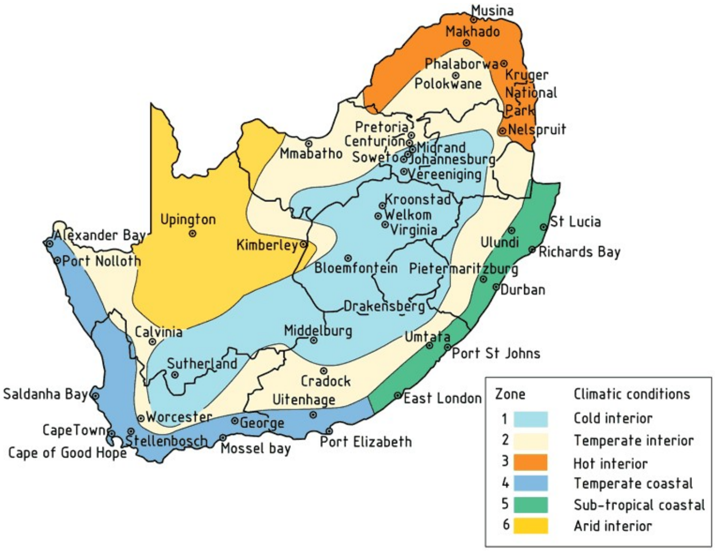

*Figure 7: location of strong winds in South Africa [14]*

Using the information stated above, the wind turbine design may be suitable for an urban environment that will merge with future energy-efficient architectural designs in buildings and is not limited to applicable off-grids in rural areas. The climatic conditions in the temperate interior such as Newcastle, Qacha's Nek (Lesotho) and Umtata will not be affected much by seasonal characteristics and the power available will be constant throughout the year. The wind speed in the temperate interior can range from 7m/s to 9m/s depending on the location as shown in Figure 8 and Table 2.

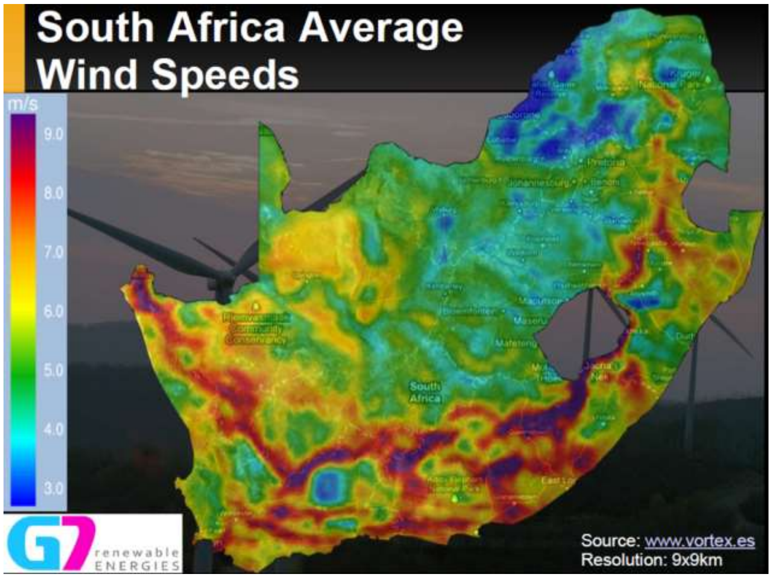

*Figure 8: South African Average Wind Speeds [15]*

**Table 2:** ***South African Average Wind Speeds [15]***

| | |
|---|---|
| North West Brits | 3m/s |
| Kruger National Park | 3m/s |
| Pretoria | 5m/s |
| Johannesburg | 5m/s |
| Port Elizabeth | 7m/s |
| Newcastle | 7m/s |
| Queens town | 7m/s |
| East London | 7m/s |

## 1.7 Research Objectives and Aims

The research aims and objectives are to understand/study the flow patterns associated with sinusoidal airfoil at the leading edge and corrugated airfoil (Optimized) qualitatively. This is to replace the conventional airfoil derived from birds wings since they have been considered to have poor aerodynamic performances in small-scale horizontal wind turbines. Although there were several previous studies on the aerodynamic performances of such corrugated airfoil, it has always been on an idealized geometry. The research gap had been identified; the idealized Bio-inspired corrugated airfoil shape used in previous studies is optimized using ANSYS Fluent Workbench-Design Explorer to determine the optimal blade profile. Similarly, the flow patterns associated with sinusoidal airfoil at the leading edge when the blade is twisted has not been considered before.

The objectives are also summarized as follows:

1. To investigate and develop a comprehensive understanding of aerodynamic characteristics of an airfoil with different wavelength and amplitude at the leading-edge at low Reynolds numbers,
2. To optimize the geometry of corrugated airfoil at the different angles of attack (AOA) ranging from 5° to 20° at chord Reynolds number $Re = 9.89 \times 10^3$ which corresponding to 2.799 m/s wind velocity at a chord length of 50.25 mm.

The aims of the current study are as follows:

1. To understand the flow patterns associated with sinusoidal airfoil and corrugated airfoil qualitatively.

2. To determine the mechanism by which Bio-inspired airfoils enhance the performance of a wind turbine.

## 1.8 Scope of work for the current research

This is a qualitative research project and it will focus on the flow behaviour of Bio-Inspired airfoils to cater for small-scale horizontal axial wind turbines. The scope of work is divided into two broad categories:

1. Bio-Inspired corrugated profiles are taken from previous studies, a two-dimensional CFD model is constructed for shape optimization process using ANSYS Fluent Workbench-Design Explorer to determine the optimal corrugated blade profile for four angles of attack (AOA) ranging from 5° to 20° corresponding to typical AOA of small-scale wind turbine blades.

   The corrugated section follows the contours of the NACA airfoils section, and since the corrugated peaks follow the contour of the filled section the effective camber and thickness will be the same and the results may be directly compared. Due to time constraints, three-dimensional simulations were not developed for Bio-Inspired corrugated profiles. Bio-Inspired corrugated study did not include wind tunnel experiments but rather compared the numerical results with results that were readily available from previous experiments.

2. Bio-inspired sinusoidal airfoil shapes were also taken from previous studies; however, the wind turbine blades were scaled-up to suit the requirements of 1KW output power. Two modified blades with variations of wavelength and amplitude were studied to investigate the aerodynamic effects at the leading edge. The results were compared to the baseline model of SG6042 airfoil, a three-dimensional CFD model results will be compared to the baseline SG6042 blade and also compared against previous work.

Computational Fluid Dynamics (CFD) software (ANSYS Fluent) was utilised for both investigations.

## 1.9 Scope limitation for the current research

The research project has the following limitations due to time constraints:

i. No tests or measurements were carried out. The findings/results are based on simulations and compared to information from the previous literature reviews,
ii. The research excludes the study of bird fatalities caused by rotating wind blades,

# 2. LITERATURE REVIEW

## 2.1. Introduction

The study of external fluid flow over a body has become a significant phenomenon, especially when designing for aerodynamic applications such as wind turbines, aeroplanes, etc. The need for flow control is mainly to achieve different engineering goals. i.e., when it comes to wind turbines applications, the external fluid studies will be done to understand the formation of the fluid-like on the wing in order to alter the parameters such as transition delay, lift enhancement, drag reduction and reducing noise.

Aerodynamic flow control devices can be considered as passive or active. Passive control almost always involves geometric alterations, such as vortex generated on geometry for flow separation control, whereas active control incorporates the use of additional energy to operate [16]. Although active flow control devices offer more advantages compared to passive flow devices, i.e., the blade is able to adjust automatically in order to accommodate the flow conditions, active flow control devices are a bit more complicated when manufacturing and maintenance is being done and this normally results in cost implications. Passive flow control is still regarded as relevant in modern designs.

Over the years, the number of airfoils was developed for the larger scale HAWTs. These airfoils were originally designed for airplane applications, applying these airfoils to small scale HAWTs result in poor performances. Airfoils designed for drones are normally applicable to small scale wind turbines [17, 18]. S822, S823, SG series are airfoils that are specially designed for small blades, and consequently, there is a need to increase their performance specifically for the ones working in variable speed mode.

Consistent with the project objectives defined, the literature review is focused on the previous studies, including aerodynamics challenges such as analysis of flow. Two very common bio-inspired shapes inspired by dragonfly wing geometries or Humpback whale fin on the leading-edge wing will be considered for the future possible horizontal axial wind turbine and will be discussed in detail in the following 2.2 and 2.3 sections.

Detailed flow behaviour between conventional smooth airfoils and Bio-inspired corrugated blades has been compared. The aerodynamic features of an airfoil have been determined using simple steady-state analyses.

## 2.2. Bio-inspired corrugated airfoil shapes for wind turbine blades

Unlike birds and conventional air planes, the cross-sectional wing profiles of many insects such as dragonflies and bumblebees are corrugated [19, 20] as depicted in Figure 9 and Figure 10. According to our current knowledge, airfoils that are conventional (Smooth) perform well at high Chord Reynolds number Re>100 000. Whereas airfoils that are not smooth (Corrugated) perform very well at low Chord Reynolds number Re= 34, 000 – 100 000.

Insects like dragonflies and bumblebees normally generate lift by a different mechanism in flight: Flapping and gliding motion. Most of the studies have been conducted in steady flow and gliding motion because most of the lift generation rely on the leading edge [26, 22, 31]. Gliding motion requires nearly zero amount of effort from the dragonfly and can travel approximately 40 times the chord lengths over one complete wing swing [26]. This advantage has led to the conclusion that pleated wings play a vital role in sustaining the aerodynamic effects.

Dragonflies Bumblebee

*Figure 9: Dragonflies and Bumblebee [19,20]*

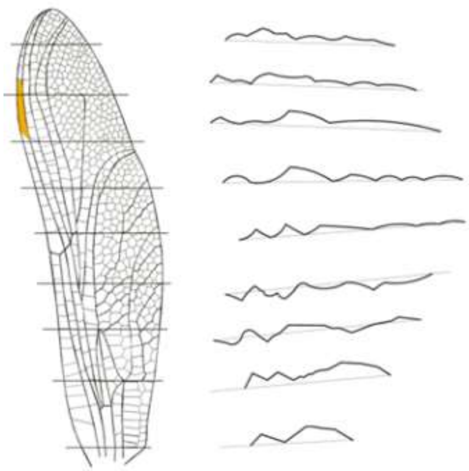

*Figure 10: Typical Dragonfly wing [21]*

The cross-sectional configuration of the dragonfly wing differs significantly along the longitudinal axis of the wing, the corrugation of the wing decreases slowly towards the wingtip. Due to the altering corrugation configuration on the longitudinal axis, also the varying angles of the leading edge, one might expect differing aerodynamic characteristics along the wing axis. Figure 10 depicts an example of a dragonfly wing cross-section, whereby these sections vary in shape. It is noted that although sections vary in shape, they all have the common two peak leading-edge.

Recent studies have shown interest in explaining the fundamental laws of the corrugated dragonfly flight aerodynamics. A corrugated airfoil at a low Reynolds number ($Re \leq 34\ 000$) has been proven to have better aerodynamic performance compared to a streamlined airfoil or flat plate.

Most of the experimental studies conducted by, Hu and Tamai [23], New et.al [24], Kesel et.al.[25], Rees [27, 28], Murphy et.al [30] and just to mention a few of them have revealed that the flow behaviour around bio-inspired corrugated airfoil results in a higher lift and a larger lift-to-drag ratio and delayed stall at higher AOA when compared to a conventional airfoil, although not studied in similar conditions. The observation from experiments shows that the smaller circulation bubbles between the notches of the corrugated airfoil will encourage the boundary layer transition from laminar to turbulent flow. Measurement has explained the flow behaviour of a corrugated wing: The peak of a corrugated airfoil acts as a tabulator to create unsteady vortex structures to encourage the transition of the boundary layer. Moreover, momentum convection between the peaks tends to provide sufficient kinetic energy in the boundary layer to overcome the adverse pressure gradient.

The primary motivation for the experimental study conducted by Hu and Tamai [23], was to investigate and compare the flow behaviour around Bio-inspired corrugated airfoil, Streamline GA (W)-1 airfoil and a flat plate at the same chord length of 101 mm. The experiment was conducted using a wind tunnel at an inlet velocity of 5.0 m/s. The performance of lift coefficient for flat plate, traditional and corrugated airfoil at Reynolds number of $Re = 3.4 \times 10^4$ were compared. The $C_L$ between 2° and 8° were comparable, the $C_L$ increases almost linearly with increasing AOA. The comparison depicted that at lower AOA(2°-8°), Bio-inspired corrugated airfoil, Streamline GA (W)-1 airfoil and a flat plate do not have much of an impact in increasing or decreasing the $C_L$. Traditional airfoil $C_L$ drops significantly when $C_L$ is above 8°, while flat plate remains constant and corrugated wing delays stall up to 12°. The $C_d$ between 2° and 14° is comparable for flat plate and GA(W)-1 airfoil whereas the drag coefficient for corrugated is higher, the $C_d$ increases.
The advantages of the bio-inspired corrugated blade at low Reynolds number are that the corrugated blade has small-scale flow separation which helps to delay stall compared to a conventional blunt airfoil. This also influences airfoil performance by producing significant aerodynamic lift over drag force, according to Newman et al. [29].

Kesel [25] results also agree with the investigations conducted by Hu and Tamai [23], Kessel analysed the lift and drag characteristics of a dragonfly forewing as shown in Figure 11 with profile cross-sections at 0.3, 0.5 and 0.7 lrel, where lrel is the relative span length. These cross-sections are compared to a flat plate, curved plate, asymmetric profile, streamline airfoil constructed by relating the peaks of respective cross-sections and corrugated airfoils.

As expected, aerodynamic characteristics obtained for wing profiles along the longitudinal axis show that results are different; profile 1 and 3 appeared to have the highest aerodynamics whereas profile 2 behaves like a flat plate. Reducing Reynolds number also shows effects in increasing the drag coefficient. The lift coefficient had further deteriorated for streamlined airfoils constructed by linking the peaks of respective cross-sections and corrugated airfoils.

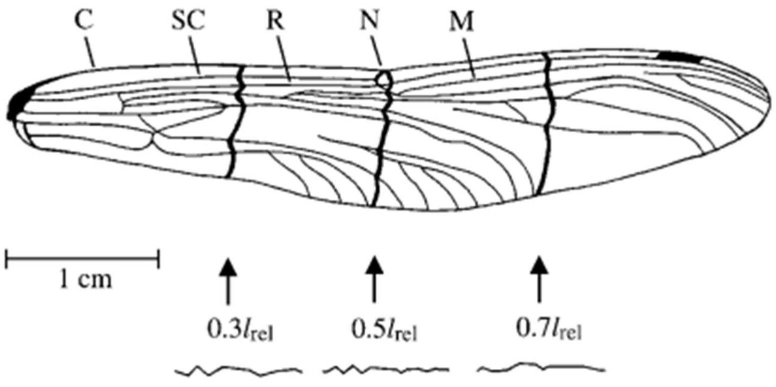

***Figure 11: Dragonfly forewing (Aeshna Cyanea) [25]***

Similarly to Hu and Tamai [23], another experiment was conducted by New et.al [24], was to study the effects of two different corrugated airfoil surface features on flow separation under similar flow conditions. The experiment was piloted using a wind tunnel and particle image velocimetry (PIV) to compare flow features at different AOA. Two different corrugated airfoils were studied; the corrugated airfoils were compared to NACA 0010 as a baseline under similar conditions.

The experiment setup was tested at Re =14000 in a wind tunnel where freestream velocity was 0.19m/s and at AOA of 0°, 10°, 15° and 20°. The observation revealed that at AOA of 0°, both corrugates profile A and B showed small trapped recirculating vortices within the peaks or at the saddle which then the flow creates an envelope over the corrugate airfoils and behaves similar to NACA 0010 profile. The trapped recirculating vortices escape from the valleys at AOA 10° for corrugated profile A, whereas for corrugated profile B this occurred at AOA 15° flow separation becomes larger and incoherent compared to NACA0010 at a similar AOA. Interestingly, at AOA 20°, the flow separation of NACA0010 profile is comparable to corrugated profiles, except that at corrugates there are multiple small scale flow separations. Corrugated profile B appeared to perform better than NACA0010 and corrugated profile A, the larger recirculating region works better than small recirculating in mitigating the flow separation behaviour.

Computational and numerical studies conducted by Vargas et.al.[26], Ho and New [31 - 32], Premachanda et.al. [33], also revealed the presence of small re-circulating regions in the corrugations.

The primary objective of Vargas et.al. [26], was to determine the flow features and the mechanism of a bio-inspired airfoil that is responsible for enhancing the performance of airfoils at low Reynolds number. The simulations for the corrugated airfoil, profiled airfoil, and the flat plate, were carried out at AOA of 0° 5° at a chord-based Reynolds number of 10,000 which matched that of Kesel et.al. [25]. Results show that the corrugated airfoil produces a 20% higher lift when compared to a streamlined airfoil. An interesting point to note is that the flat plate generates the biggest drag at AOA of 5.0° due to a huge leading-edge stall.

Ho and New [31, 32], investigated the aerodynamic and flow characteristics of two bio-inspired airfoils similar to the experiment conducted by New et.al [24]. An unsteady, two-dimensional simulation was conducted using the commercial software ANSYS Fluent 14.5 ( SST-k-w model) at a chord Reynolds number of 14 000. Results were compared to NACA0010 at various AOA. At AOA 0° vortices are shown but appeared to be trapped or moving at a low speed for both corrugated airfoils. This resulted in creating an airstream envelope across corrugates that behaves similar to NACA0010 airstream, the performance of all scenarios is more or less comparable. AOA20°, it is apparent that flow separation increases with the AOA. interestingly, corrugated airfoils show smaller bubbles compared to NACA0010 at the same AOA, Corrugated A has two bubbles, the smaller bubble residing just upstream mid-chord while a significantly larger one at the downstream end. Corrugated B and NACA airfoils, however, have one large bubble that is not detaching. The aerodynamic performance varies across and corrugated airfoils has advantages when it comes to lift to drag ratio.

Another similar research [33] was undertaken on the effect of wing corrugations on the aerodynamic performance of low Re number, the investigation used the commercial finite solver Fluent 12.1 to solve the unsteady incompressible Navier Stokes equation using a pressure-based and SIMPLE algorithm. Corrugated airfoil was compared to a flat plate and NACA006 and NACA012. Results indicated that the thinner wings produce higher lift force, and for corrugated regardless of the thickness, the downward-facing edge produces slightly more lift force. The flat plate section was appropriately the same as corrugated wing section.

Majumdar [34] stated that the generation of vortices is formed due to a pressure difference between fluid and the surface. The pressure difference is created due to the collision of two linear wind jets; one wind jets is weaker than the other, this will create a random velocity field in the space-time continuum accompanied by a chaotic occurrence of vortices. Also, vortices can be generated due to surface discontinuities; the flow will separate from the mainstream flow, resulting in a separated region of flow. An experiment conducted by Yarusevych et al. [35] on vortex shedding from an airfoil in low Reynolds number also shows the flow behaviour in an airfoil shape. The experiment was conducted considering two regimes: boundary layer separation without reattachment and separation bubbles formation. The unsteadiness between these two regimes depends on the range of Reynolds numbers and angle of attack, at low Reynolds numbers the separated shear layer fails to reattach from the airfoil and a wide wake will be formed, while at high Reynolds numbers a turbulent separated shear may reattach. The experiment was performed in a wind tunnel. The main objective of the experiment was to gain a basic understanding of boundary layer and wake development at the range of Re ($55 \times 10^3 \leq Re_c \leq 210 \times 10^3$) and three angles of attack 0°, 5°, and 10°. For $Re_c = 55 \times 10^3$ and $Re_c = 100 \times 10^3$, the boundary layer at the upper surface of the airfoil separates and a wide wake is formed, and in $Re_c = 150 \times 10^3$ the shear layer reattaches and remain attached at the trailing edge. The experimental results also show that the roll-up vortices are directly proportional to the Reynolds number increases.

The superior performance on corrugated blades is yet to be fully understood. One theory is that airflow on a corrugated airfoil gets stuck between the peaks where it can rotate slowly or be stagnant, these results corrugated acting as a conventional blade [28], In addition, the trapped vortices draw flow towards the airfoil surfaces thus reducing separation. These hypotheses were later studied computationally by Abel and Rajat [26], and the results were in line with Rees conclusion [28].

Although there is a number of previous studies on the aerodynamic performances of such corrugated airfoil, it has always been on an idealized geometry. The purpose of this research is to find an optimised corrugated profile in terms of improved aerodynamic performances. The idealized Bio-inspired corrugated airfoil shape used in previous studies is optimised using ANSYS Fluent Workbench-Design Explorer to determine the optimal blade profile. It serves as an initial study towards the investigation of such corrugated bio-inspired airfoils for use on small scale wind turbine blades.

## 2.3. Bio-inspired sinusoidal air-foil shapes for blades

Unlike conventional smooth airplane airfoils, the profiles of humpback whale flippers have tubercles along the leading edge. Tubercles are rounded protuberances that alter the flow-field around the wing. Investigations based on the effect of leading-edge tubercles in two dimensional and three-dimensional configurations have previously been conducted on wings, These tubercles act as lift improvement devices, by allowing longer flow attachment at a bigger range of AOA, thus resulting in stall delaying whilst increasing lift coefficient [36, 38]. Humpback whale flippers have been hypothesized to provide benefits that allow whales to navigate in much shallower water, thermoregulations as heat dissipater, reduce acoustics and increase manoeuvrability [36]. More detailed studies are discussed in the subsequent sections.

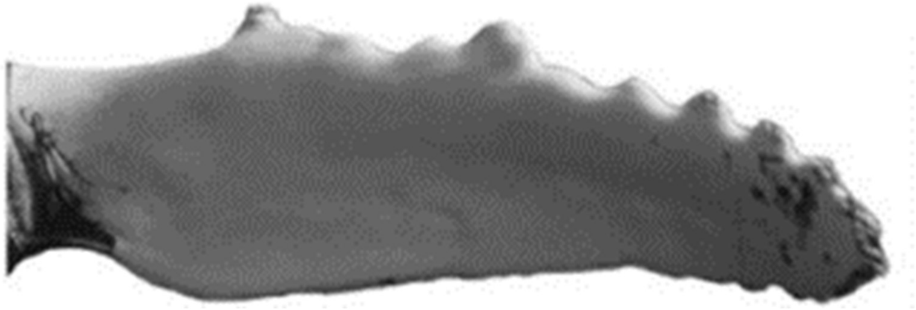

*Figure 12: Typical Humpback Whale Wing with Tubercles at the leading edge [37]*

The tubercle effect contributes significantly to the aerodynamics of wings, these tubercles have been reported to be of great significance in designing applications with Reynolds numbers comparable to the ones of a humpback whale such as, ventilation fans, aircraft, windmills and watercraft. [36, 41].

The leading-edge tubercles serve as passive-flow control devices which enhance the flippers performance and manoeuvrability. The aerodynamic performance is enhanced because of counter-rotating vortices created as a result of integrating tubercles into lifting surface and resulting in flow separation delay.

The experimental studies conducted by, Miklosovic et.al [38], Bai et.al [39], Bolzon et.al [40], Goruney et.al [42], Fish et.al [36] and many more have confirmed that the leading tubercle wings are capable of achieving better performance compared to blades without tubercles. For the purpose of results interpretations, it should be noted that most of these flow field experiments were carried out on a simplified rectangular airfoils configuration at the leading edge.

The experimental study conducted by Miklosovic et.al [38] using a wind tunnel to compare measurements of lift and drag between two models of humpback flipper; Smooth and tubercles at the leading-edge shows that the stall of a smooth model occurs at an angle of attack (AOA) of approximately 12° whereas for a tubercle model the stalling occurs at AOA approximately 18°. The drag coefficient of the tubercle model was not more than the baseline model at AOA 12°<AOA<17° by approximately 23.8 % and approximately 12.5% at AOA 10°<AOA<12°. Below 10° Cd is comparable. The introduction of tubercles at the leading-edge has delayed the stall at higher angle of attack (AOA) by approximately 40%, while increasing total lift without significantly increasing drag, the aerodynamic performance increased by 6% compared to the smooth model and the analogy has been drawn that the passive flow serves as a beneficial approach in flow by generating vortices that increase momentum exchange in the boundary layer.

Performance effects for tubercles at the leading edge were also studied by Bai et al. [39] using wind turbine experiment at wind speeds of 6, 8 and 10m/s. This was conducted at various angles of attack ranging from 0° to 50°. The test was conducted for four modified models with different wavelength and amplitude at the leading-edge. these models were respectively compared to a baseline model that has a smooth leading edge. The tip speed ratio range and the Reynolds number range were 2-7 and 28 000 – 440 000 respectively. The experiment revealed that the modified blade with smaller amplitude and wavelength has a better power coefficient compared to the baseline blade at low Reynolds numbers whereas blades with bigger wavelength and amplitude are more suitable for high Reynolds numbers due to the recirculation around the tubercles.

The results from Bai et al, agree with Goruney et.al [42], on his experiment for a delta wing flow with a sinusoidal leading edge at higher AOA (50°). He observed that when the ratio of the wavelength to amplitude is maintained at a smaller value it is more effective close to the surface topology, tubercles with amplitude of at least 4% the of wing chord counteract the large-scale three-dimensional separations.

Zhang and Wu [41], conducted a computational simulation using a commercial software Fluent to analyze the aerodynamic performance of modified blades. Five cases with different amplitude and wavelength were compared to NREL phase-VI baseline geometry. Five kinds of speed 7, 10, 15, 20 and 25m/s were calculated for all kinds of cases. results reveal that more robust power output is produced between 10 – 20m/s on all modified cases.

The superior performance of these leading-edge tubercles is not yet fully understood. One hypothesis is that these tubercles can modify the hydrodynamic characteristic to increase the effectiveness in turning [43].

Even though there were many studies conducted on the aerodynamic performances of such tubercles at the leading edge, the effects due to twisted blades have not been considered yet. The purpose of this research is to study the effects of airfoil tubercles on a small-scale horizontal axis wind turbine. It serves as an initial study towards the investigation of such airfoils for use on small scale wind turbine blades.

# 3. METHODOLOGY

## 3.1. Introduction

Computational Fluid Dynamics (CFD) is a simulation tool, which uses applied mathematics to model flow situations for the prediction of heat, mass and momentum transfer in the industrial process, environmental applications and physiological applications [44, 45]. The growth of CFD is associated with the advancement of high-speed computers, and initially, it was used to make numerical techniques for solving problems related to national defence then later used for additional scientific and engineering applications. [45].

Navier Stokes equations govern the motion of viscous fluids and are the most straightforward method used to tackle the fluid dynamic problem within appropriate boundary conditions. Some of the advantages of using CFD is that it allows for evaluation of geometric changes with lesser effort and is thus cost-effective, instead of using laboratory testing which have scale up inaccuracies, on the other hand the model is based on fundamental physics and are scale-dependent [45].

CFD packages are not suitable for fluids that are not treated as a continuous field of properties. i.e., extremely rarified gas cannot be accurately modelled using Navier Stokes solver. There is a limitation in using commercial CFD packages, the limitation is indicated in Figure 13 for values of Kn lower than 0.3, i.e., when the mean free path is less than 30% of the body length, the NS (or Euler) equations are applicable.

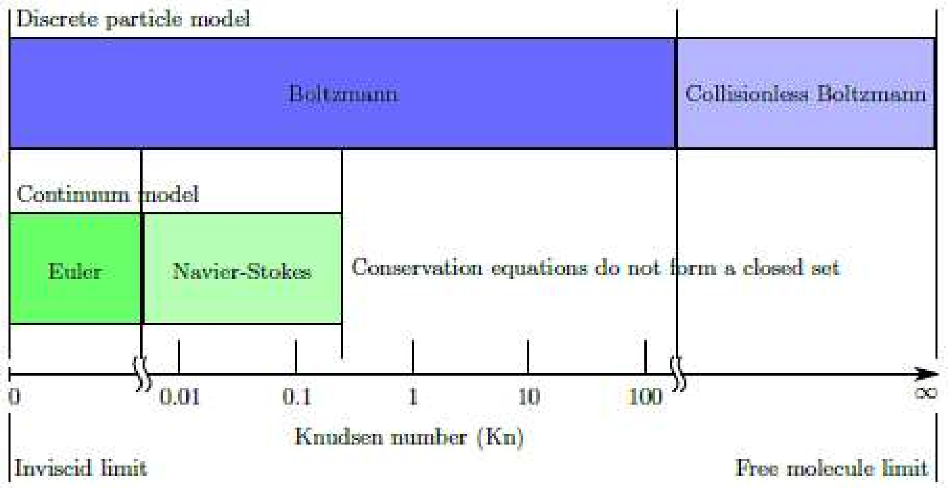

**Figure 13: Ranges of applicability in terms of a Knudsen number [46]**

The range of applicability is calculated below using Knudsen number,

$$Kn = \frac{\lambda}{L} \tag{3.1.1}$$

$$\lambda = \frac{V/N}{4\pi\sqrt{2}r^2} \tag{3.1.2}$$

$$M = \frac{V}{a} \tag{3.1.3}$$

$$V = \frac{nRT}{P} \tag{3.1.4}$$

Where,

Kn = Knudsen Number

L = Characteristic length

$\lambda$ = Mean Free Path Length

V = Volume [$m^3$]

N = Molecules (1 mole = 6.02x $10^{23}$ )

r = 1.5 x $10^{-10}$ Particle molecule radius [m]
n = Number of Moles [mol]

$R_u$ = Specific Gas Constant (8.31447 $\frac{KJ}{K}.mol.K$)

P = Atmospheric Pressure [Pa]

The Knudsen number for Bio-inspired corrugated airfoils, where the design parameters are given below:

P = 88 Kpa

T = 300 K

L = 0.0569 m

$\gamma = 1.4$

$M = 0.0086 \quad Incompressible\ flow$

$V = 0.0283m^3$

And

$\lambda = 1.17753\ x\ 10^{-7}m$

Therefore

$Kn = 2.069\ x\ 10^{-6}$

Knudsen number for Bio-inspired sinusoidal airfoils, where the design parameters are given below:

P = 101.3 Kpa

T = 300 K

L = 0.51 m

$\gamma = 1.4$

$M = 0.02 \quad Incompressible\ flow$

$V = 0.0246m^3$

And

$\lambda = 1.0219\ x\ 10^{-7}m$

Therefore

$Kn = 2.0\ x\ 10^{-7}$

ANSYS fluent will be used to simulate the flow around airfoils objects and with its capabilities, it also offers much flexibility and power which enables it to provide complete simulation processes such as flow problems, post-processing across a very broad spectrum of processes such as turbulent flows, heat transfer, acoustic modelling, and chemical species mixing and reaction, etc.

The study will use 2D simulation to optimize the shape of Bio-inspired corrugated airfoils whereas 3D simulation will be used for Bio-inspired sinusoidal airfoils.

## 3.2. CFD Steps

When using CFD to analyze flow fields, there are three general steps to be followed: Preprocessing, Solving, and Post-Processing as shown in Figure 14. Pre-processing includes the sketching/importing of geometry, Geometry modification, and meshing. The mesh is the system of nodes that describes the geometry of the flow field and also serves as computation points for the solution of the governing equations. The second step is the solver, this is where the geometric representation by the mesh is passed to the solver, along with information detailing conditions at certain points in the domain known as boundary conditions. It is the solver that simulates the variation of the flow variables throughout the domain based on these boundary conditions. Post-processing is when the data produced by the solver is formatted in such a way that useful information about the flow field being analysed.

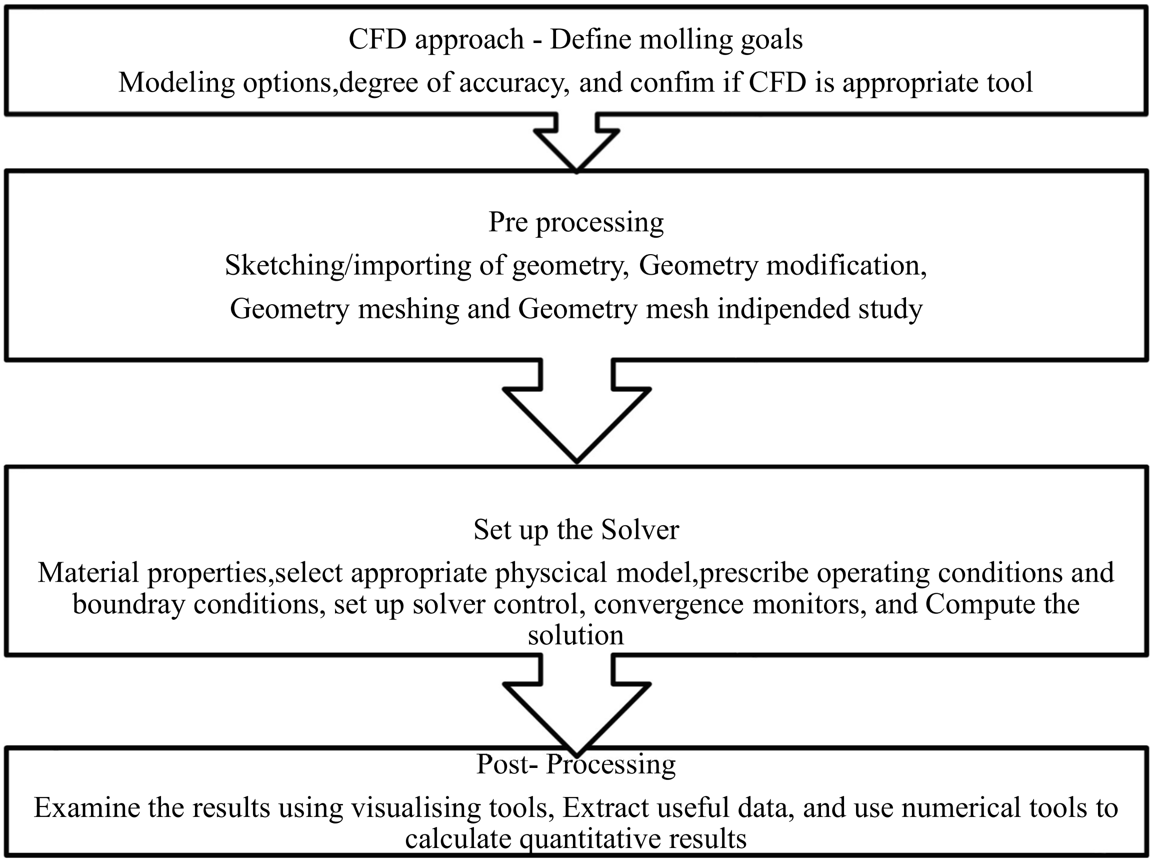

*Figure 14: CFD process flow diagram*

## 3.3. CFD Method - Bio-inspired corrugated airfoils

A two-dimensional rigid corrugated blade was modelled in ANSYS Fluent 17.1 using Workbench Design Explorer at Reynolds number Re = $9.89 \times 10^3$ corresponding to 2.799 m/s wind velocity, which is the lowest wind velocity in Johannesburg according to European Wind Energy consulting company Vortex [15] with a chord length of 50.25 mm. The optimization was performed on AOA of 5, 10, 15 and 20° as these are the AOA present in the baseline wind turbine blades that would be used for the next study.

### 3.3.1. Geometry and Boundary Conditions

The geometry and boundary conditions used for the bio-inspired corrugated blade are shown in Figure 15, Figure 16 respectively. The geometry is a corrugated cross-section of a dragonfly wing taken from Ho and New [32]. The fluid domain width is 20 C, where C is the blade chord, all around the blade. An exercise to determine the necessary domain size was conducted and is shown below.

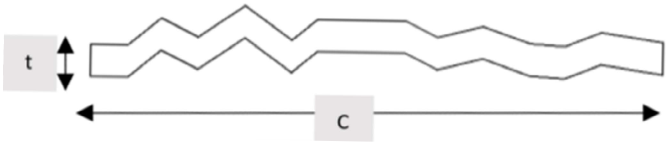

*Figure 15 : Corrugated blade geometry (C= 50.3mm; t=2mm)*

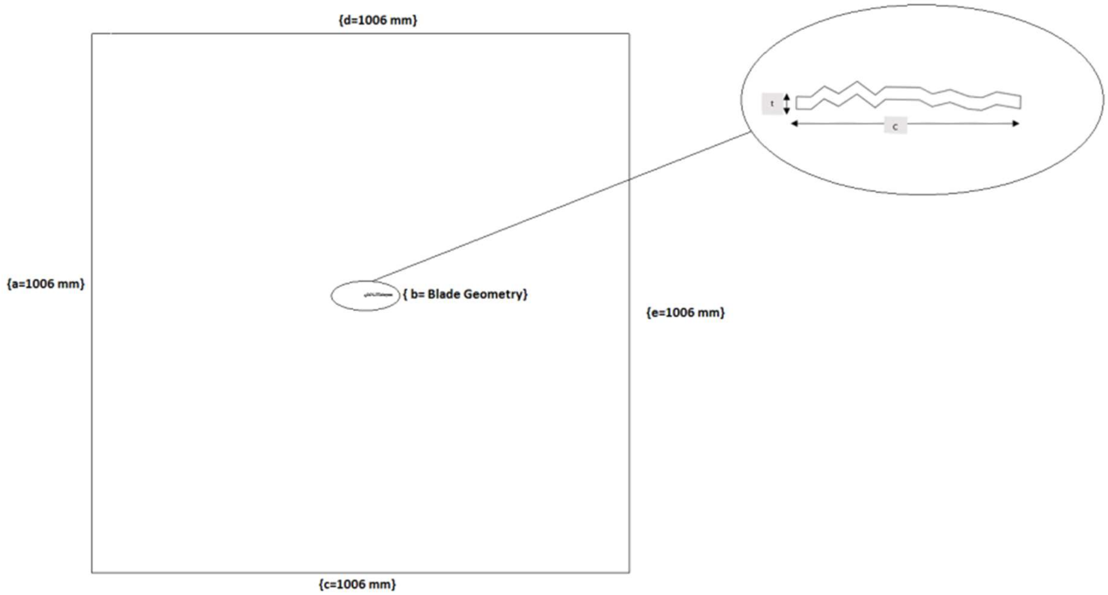

*Figure 16 : Boundary Conditions {a}, Uniform Velocity inlet normal to boundary {b}, No slip wall {c}, Pressure inlet {d}, pressure outlet{e}.*

Quadrilateral unstructured meshing was used with inflation layers as depicted in Figure 17 and Figure 18. The maximum aspect ratio (AR) of the chosen mesh was 6.2. The inflation layers were introduced to capture all the boundary effects near the wall of an airfoil, using viscous sublayer approach.

Resolving the viscous sublayer, first grid cell height was calculated from the following equations,

$$Re_L = \frac{\rho V L}{\mu} \tag{3.3.1}$$

Where,

L = Characteristic length [m]

V = Velocity [m/s]

$\rho$ = Density [kg/m$^3$]

$\mu$ = Dynamic Viscosity [kg/ms]

$$Re_L = \frac{\rho V L}{\mu} = \frac{1.225 kg/m^3 \; x \, \frac{2.799m}{s} \; x \; 0.05025}{1.8 \; x \; 10^{-5} kg/ms}$$

$$Re_L = \; 9.571 \; x \; 10^3$$

$$C_f = 0.058 \; (Re_L)^{-0.2} \tag{3.3.2}$$

$$C_f = 0.058 \; (9.571 \; x \; 10^3)^{-0.2}$$

$$C_f = 0.0093$$

$$\tau_\omega = 0.5 \; C_f \rho (V)^2 \tag{3.3.3}$$

Where,

$\tau_\omega$ = Wall Shear Stress [kg/ms2]

Cf = Skin Friction Coefficient

ρ = Density [kg/m3]

μ = Dynamic Viscosity [kg/ms]

V = Wind Speed [m/s]

Therefore,

$$\tau_{\omega} = 0.0446 \text{ kg/ms2}$$

$$U_{\tau} = \sqrt{\frac{\tau_{\omega}}{\rho}} \qquad (3.3.4)$$

Where,

$\tau_{\omega} =$ Wall Shear Stress [kg/ms2]

ρ = Density [kg/m3]

$$U_{\tau} = 0.193\, m/s$$

$$Y^{+} = \frac{\rho U_{\tau} Y}{\mu} \qquad (3.3.5)$$

Where,

ρ = Density [kg/m3]

μ = Dynamic Viscosity [kg/ms]

$U_{\tau}$= Velocity [m/s]

Y = First Layer height [m]

$Y^{+} \approx 1$

$$Y = 7.43\, x\, 10^{-5} m$$

The first layer height was set to 0.06 mm and the maximum y+ was 1.45. The inflation growth rate was set to 1.2. A low cell growth rate was used on the domain to allow a finer mesh in the vicinity of the blade. A finer mesh as showed in Figure 18 was required behind the blade to accurately capture magnitudes of derived values such as vorticity in the von Karmen vortex sheet which tend to become diluted due to averages occurring in larger meshes. The presence of the finer mesh also promotes more accurate results in this region of interest. Mesh morphing (Meshing sizing command) was enabled to aid during mesh independent study and shape optimization.

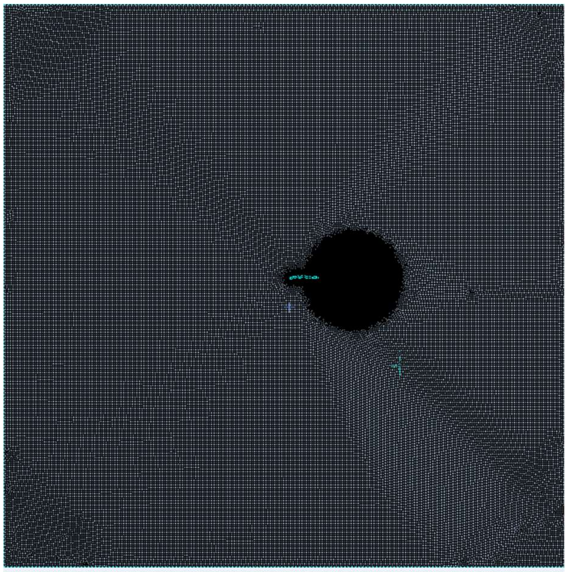

Figure 17: Fluid Domain Mesh

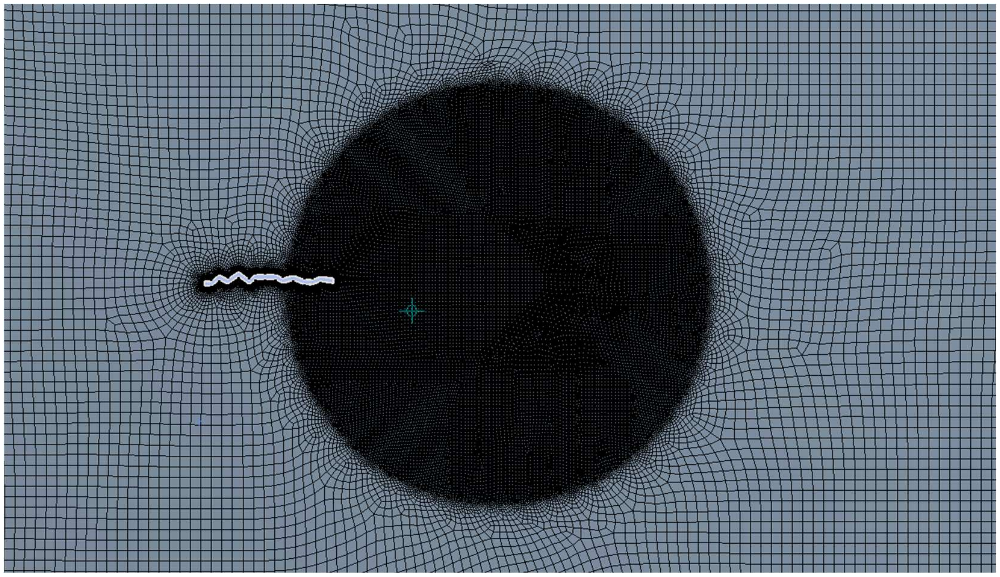

Figure 18: Finer Mesh at the Trailing Edge of the Blade

Several meshes were refined and tested to make sure the mesh resolution doesn't affect the solution. The level of the grid is evaluated using Richardson extrapolation [47] and the study shows that the finest grid solution has a grid convergence of less than 5%. The findings from these stages were then compared and when the results of interest are not changing within an acceptable tolerance the model can be said to be mesh independent.

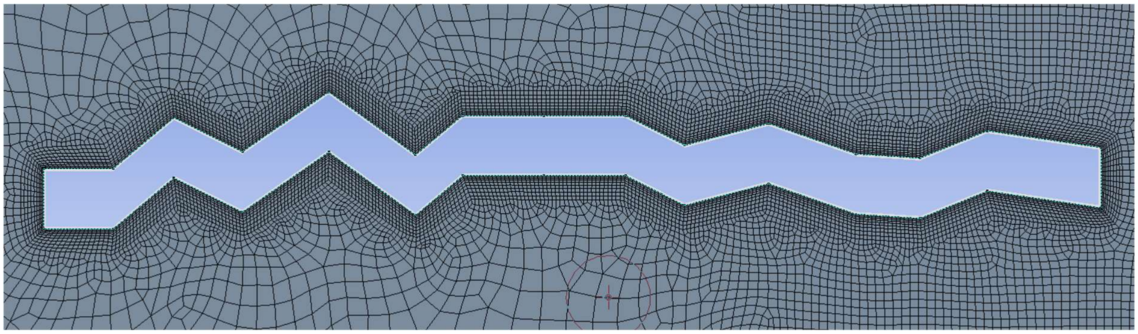

Figure 19 : Local mesh around the blade

The second stage of mesh independence was done to assess the necessary number of inflation layers as shown in *Figure 19*, the results are shown in Table 4. Although the results obtained 3 layers and 7 layers are very close, Mesh 2 was eventually used.

The mesh independence of the fluid domain was also conducted as can be seen from Table 5, the appropriateness is within an acceptable range.

**Table 3: First stage mesh independence result**

| | AOA | Number of Elements | $C_L$ | $C_D$ | % difference in $C_L$ | % difference in $C_D$ |
|---|---|---|---|---|---|---|
| Mesh 1 | 5° | 40355 | 0.079 | 0.096 | | |
| Mesh 2 | 5° | 198932 | 0.162 | 0.079 | 0.512% | -0.177% |

**Table 4: Second Stage mesh independence result**

| | No. of Inflation Layers | Number of Elements | $C_L$ | $C_D$ | % difference in $C_L$ | % difference in $C_D$ |
|---|---|---|---|---|---|---|
| Mesh 2 | 7 | 198932 | 0.162 | 0.079 | | |
| Mesh 2A | 3 | 196239 | 0.164 | 0.079 | 0.012% | 0% |

**Table 5: Mesh independence result for the fluid domain**

| | | Number of Elements | $C_L$ | $C_D$ | % difference in $C_L$ | % difference in $C_D$ |
|---|---|---|---|---|---|---|
| Domain 1 | 20 C | 198932 | 0.162 | 0.079 | | |
| Domain 2 | 10 C | 150390 | 0.160 | 0.081 | -0.013% | 0.025% |

The pressure-based solver was utilised to model the flow around the blade. The proposed `solver was used because bio-inspired corrugated blades are studied at low Reynolds number. SST (k-omega) turbulence model was used since flow recirculation or flow separation is the dominant feature in the flow. The fluid used is air at a standard sea-level density of 1.225

kg/m3. Turbulence intensity at the inlet was set to 1.1 % and turbulence viscosity ratio was 10. Pressure-velocity coupled with gradients was set to least squares cell-based. The velocity inlet for various AOA is summarized in Table *6*.

**Table 6: Boundary Conditions Velocity Inlet**

| | AOA 5 | AOA 10 | AOA 15 | AOA 20 |
|---|---|---|---|---|
| | | | | |
| Reference Frame | Absolute | Absolute | Absolute | Absolute |
| Velocity Magnitude | 2.799 m/s | 2.799 m/s | 2.799 m/s | 2.799 m/s |
| X-component of Flow Direction | 0.996 | 0.984 | 0.966 | 0.9396 |
| Y-component of Flow Direction | 0.087 | 0.174 | 0.259 | 0.342 |

The proposed Pressure, momentum, turbulent kinetic energy and specific dissipation rate equations were solved using the second order-upwind convection scheme. The pseudo transient solution was used to lead to better convergence as the flow is inherently unsteady. Pseudo-time step set to 0.01(s) and Convergence residuals were set to $10^{-5}$, however, the solution was only deemed to be converged when CL and CD have converged to a stable value.

### 3.3.2. Shape Optimisation

There are two different ways to perform shape optimization in ANSYS workbench [48]: One of the methods is to parameterise the geometry in design modeller and then perform a parametric analysis. This method uses a what-if scenario in the design explorer tool in the workbench to optimize the design and it is based on the objective function using methods like the design of experiments (DOE), correlation, response surfaces, and direct optimization. The second method uses the adjoint solver in fluent where the shape is morphed based on the specified objectives, using this method there is less restrictive as it does not require the geometry to be parametrized. Both methods are suitable, however, for the present work the design explorer tool was used simply because in many cases the adjoint solver produces shapes that are difficult or costly to manufacture. Parametric analysis method has advantages to provide better control over the optimization procedures.

Design explorer is an effective tool for designing and understanding the analysis of parts and assemblies. This is one of the best ways of understanding some of the engineering challenges. The Design explorer assists in determining the key parameters influencing designs and can also assist in acquiring the conditions for optimal performance. Design explorer is a scientific method to conduct experiments with a given set of parameters, using boundary settings to minimise the runs required to understand the influence of these parameters.

The Design explorer has different types of algorithms namely, Optimal Space-Filling Design (OSF), Central Composite Design (CCD), Box-Behnken Design, Custom, Custom sampling, Sparse Grid initialization and Latin Hypercube sampling design (LHS). The types of design explorer depend on the number on design points required for accurate results. An application that requires the coverage of extremes or even distribution in algorithm, CCD, Custom and Box-Behnken are recommended DOE types. Whereas application requires non-linear response, Sparse Grid, OSF, and LHS are recommended DOE types. There advantages and dis-advantages are listed in the appendix B.

The corrugated blade has 14 nodes on the top and bottom surfaces and in total, the blade has 28 nodes as shown in Figure *20*. To comply with the CCD DOE requirements, fewer effective nodes were ignored. Nodes, where the wing is more flattened did not appear to have any impact in improving lift [24]. Unimportant input parameters were excluded to reduce unnecessary sampling points. The location of the first 10 nodes have been selected as the effects of regions closer to the trailing edge is expected to contribute less to the overall aerodynamic performance.

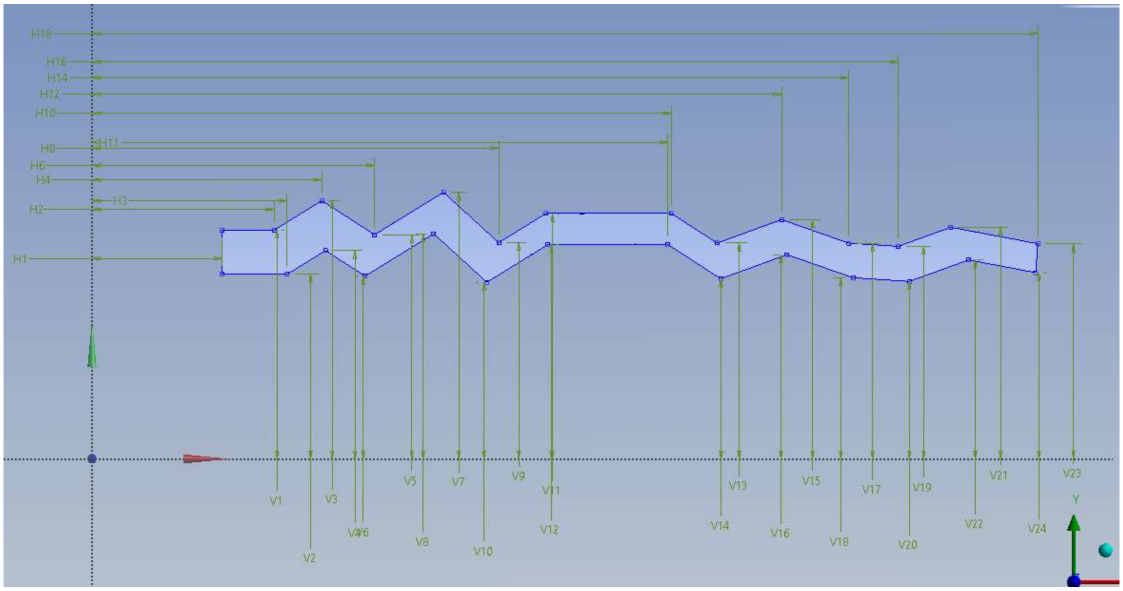

**Figure 20: input parameters**

Inputs were selected in a manner to avoid over constraining. Parametric expressions as shown in Appendix A were set to link lower and upper limits and to restrain the nodes not to change more than 30% towards the adjacent node. 30% change of nodes towards the adjacent nodes has been selected after several trial-and-error approaches in determiningthe proper parameters to achieve the goal without constraining the model. Nodes had four degrees of freedom of movement, two (negative and positive) in the X and Y axis each.

Appendix A shows the breakdown for parametric expression procedures. The parametric expressions were set to achieve four degrees of freedom two (negative and positive) in the X and Y axis each CFD Method - Bio-inspired sinusoidal airfoil.

## 3.4. CFD Method- Bio-Inspired Sinosoidal airfoil

SG-airfoils are proven to perform better when compared to NREL airfoils for small horizontal axial wind turbines [17]. These airfoils are intended primarily to capture power ranging from 1KW to 5KW for both conventional (tapered or twisted) blades.

Locations such as Port Elizabeth, Newcastle, Queens town and East London are classified as climatic zones 4 and 5 ( Figure 7: location of strong winds in South Africa [14]) in South Africa, they have been confirmed to have an average wind speed of 7m/s [15]. Design parameters are set and the objectives is to achieve 1Kw output power for small horizontal wind turbines.

Depending upon the particular usage or the type of occupant to which a building is intended for and the activities, the minimum lighting and equipment electrical load level is determined in accordance with South African National Standard (SANS) [14], using efficient methods in contrast with SANS 204: 2011. An appropriate method of cost-benefit analysis was carried out in order to provide energy-efficient in buildings. The estimated maximum energy demand and energy consumption for a dwelling house is provided below in Table *7*.

**Table 7: Estimated power for Household Electric Appliance**

| Appliance | Power use (watt) | Hours/day in use | Number of appliances | Battery Capacity (kwh) |
|---|---|---|---|---|
| light bulb - Incandescent | 60 | 4 | 1 | 0.24 |
| Electric Motor gate | 450 | 0.15 | 1 | 0.0675 |
| Security Systems | 120 | 4 | 1 | 0.48 |
| **Electricity consumption total** | **630** | **6** | **5** | **0.78** |

Table *7*, depicts that the total consumption for a day is estimated to be 0.78 Kwh which is below objectives to achieve 1Kw output power for small horizontal wind turbines. Selecting

SG6042 airfoil, the applicable coefficient of performance (Cp) was taken as 0.4 completed with a tip speed ratio of 6. The density of air is 1.23kg/m3.

Hand calculations of the expected results are shown in Table 8. These results will be compared with the simulation results for verification and validation.

**Table 8: Hand calculations of expected results**

| | Symbol | Equation | Units | Baseline Model |
|---|---|---|---|---|
| Power captured by Rotor blades from Wind | P | | KW | 1 |
| Wind Speed | V | | m/s | 7 |
| Coefficient of Performance | Cp | | | 0.4 |
| Tip speed ratio | λ | | | 6 |
| The density of Air | ρ | | Kg/m3 | 1.23 |
| Span of Turbine Blades (or radius) | r | $r = \sqrt{\frac{2P}{\pi \times Cp \times \rho \times V^3}}$ | m | 1.95 |
| Omega | $\frac{\omega 1}{\omega 2}$ | $\omega 1 = \frac{\lambda V}{r_{-}}$ | $\frac{Rad/s}{RPM}$ | $\frac{21.58}{206.08}$ |
| Torque | T | $T = \frac{P}{\omega}$ | Nm | 46.34 |
| Lift Force on Single Blade | FL | $FL = \frac{T/3}{moment\ arm} = \frac{T/3}{1/3 \times r_{-}}$ | N | 23.83 |
| Calculated Coefficient of Lift on Turbine Blade | $C_L$ | | | 2.27 |
| Measured plan area of a Wing | S | | $m^2$ | 0.35 |
| Average Chord | c | $c_{-} = \frac{A}{r_{-}}$ | m | 0.18 |
| Chord/Radius | | | | 0.09 |
| Dynamic Viscosity | $\mu$ | | | 1,80E-05 |
| Reynolds Number | | $Re = \frac{(\rho\ x\ V\ x\ L\ )}{(\mu)}$ | | 2,43E-05 |
| Gauge pressure | P | | Pa | 8.6E+04 |
| Temperature | T | | K | 300 |
| The ratio of specific heat | $\gamma$ | | | 1.4 |
| gas constant | R | | J/kg. K | 287 |
| Sound Speed | a | $a = \sqrt{\gamma}\mathrm{RT}$ | m/s | 347.19 |
| Mach number | M | | | 0.02 |
| Taper ratio | TP | $\frac{Chord\ \ tip}{Chord\ root}$ | | 0.4 |
| Tapered wing | | $\mathbf{C(y)} = \frac{2A}{91+TP)r}[1-\frac{1-TP}{r}\|y\|$ | | |

The analysis of power estimate is simply estimated by using one-dimensional momentum theory using the assumptions below:

1. Incompressible flow,
2. Steady flow,
3. Homogeneous flow,
4. No flow rotation on the blades,
5. The static pressure far upstream and downstream of the rotor is equal to the undisturbed ambient pressure,

The turbine aerodynamic power output can then be expressed by the following equation,

$$P = \frac{1}{2} C_p \rho A V^3 \tag{3.4.1}$$

Where,

P = wind power [Kw]

Cp = 0.4

$\rho$ =1.225kg/m$^3$

$A = \pi r^2$[m$^2$]

V = 7 m/s

$$P = \frac{1}{2} \times 0.4 \times (\frac{1.225kg}{m3}) \times \pi \times (1.95m)^2 \times (7m/s)^3$$

$$P = 1KW$$

The velocity at the blade tip should be

$$V = \omega r$$

$$V = -21.58\, rad/s \times 1.95m$$

$$V = 42.081\, m/s$$

Where,

r = blade length 1.95m

$\omega$= angular Velocity -21.58 rad/s

### 3.4.1. Geometry

Baseline SG6042 data file was imported to Qblade v0.963 software and the model was generated. Qblade is a software used for wind turbine blade designs as well as quick simulation. For this particular study, Qblade will be used for blade design. Out of four airfoils that were designed and tested by Giguere et al. [17] in wind tunnel, SG6042 was chosen because its Reynolds number corresponded with the current case study.

The Dat.file of SG6042 airfoil was imported to Qblade software to construct the 3D wind turbine blade. Three-dimensional wind turbine blades were constructed. Because Qblade can only export models in stl or 3D points, option for points was viable since the models required some modifications. Modifications were done using AutoCad inventor software to generate and refine the final CAD models.

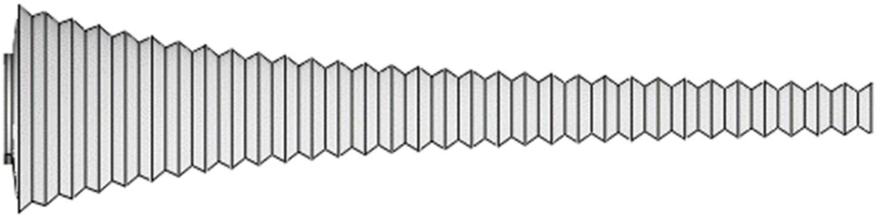

Figure 21: QBlade Geometry before being exported

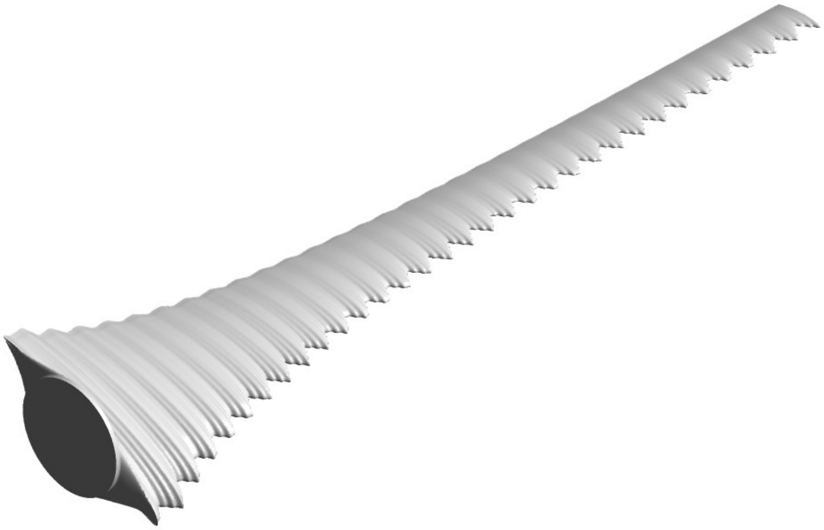

Figure 22: Typical Modified Geometry

Figure 21 indicates the geometry model before being exported and as can be seen, the geometry had sinusoidal shape in both the trailing-edge and leading-edge. The model further shows some bumpy shape at the upper side of the blade, this is due to twisted and tapered blade. The primary intention for the geometry was to study sinusoidal effects at the leading-edge. The model was exported to AutoCad inventor for further refinery, its apparent on Figure 22, a sinusoidal shape is only at the leading-edge of the blade. due to tapered and twists of the blade, the modified geometries still show the sinusoidal shape at the upper side of the blade.

To eliminate errors during meshing or to avoid jagged bodies (As shown in *Figure 23*) which might have resulted in inaccurate results, the geometry was sliced a small portion parallel to the trailing and leading edge in order to leave a very small face on the blade. With a small face, a local mesh is feasible. The 3D models including the baseline are shown on, Figure 24, Figure 25, and Figure 26. The modified models were inspired by Bai et al. [39]. where he concluded that modified blades with smaller amplitude and wavelength have better power coefficients. For this instance, two modified models' parameters are shown in Table 9 where model-1 with smaller amplitude and wavelength and Model-2 with larger amplitude and wavelength are illustrated. Qblade v0.963 software enhanced the blade by introducing a tapered shape and twist on the *airfoil*.

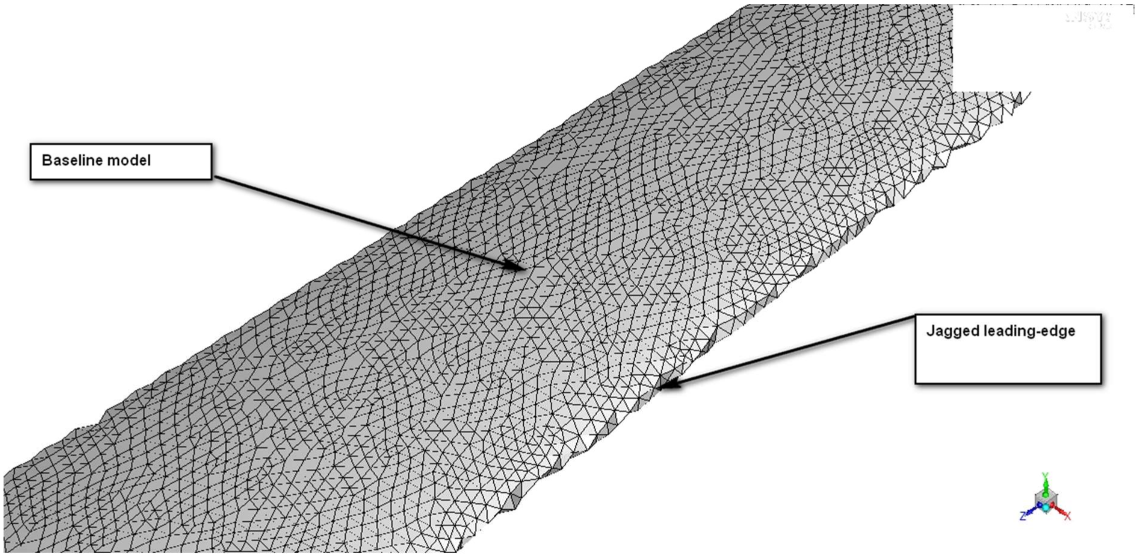

***Figure 23 : Baseline model jagged at leading edge***

**Table 9:** ***Modified blade models at average chord***

| | Baseline Model | Modified model 1 | Modified model 2 |
|---|---|---|---|
| Amplitude | - | 4% of the chord | 11.9% of the chord |
| Wavelength | - | 14.3% of the chord | 40.4% of the chord |

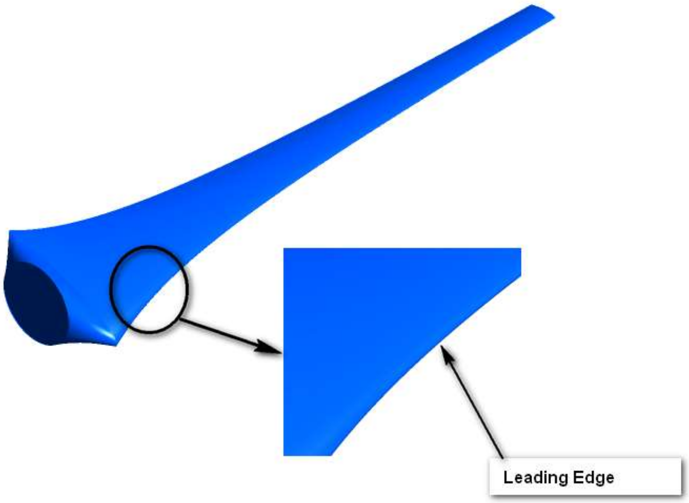

**Figure 24: Geometry model- Baseline**

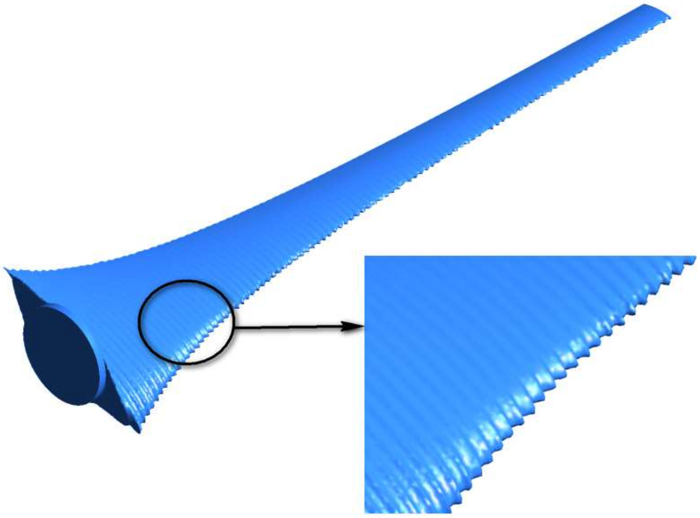

**Figure 25: Geometry model- Model-1**

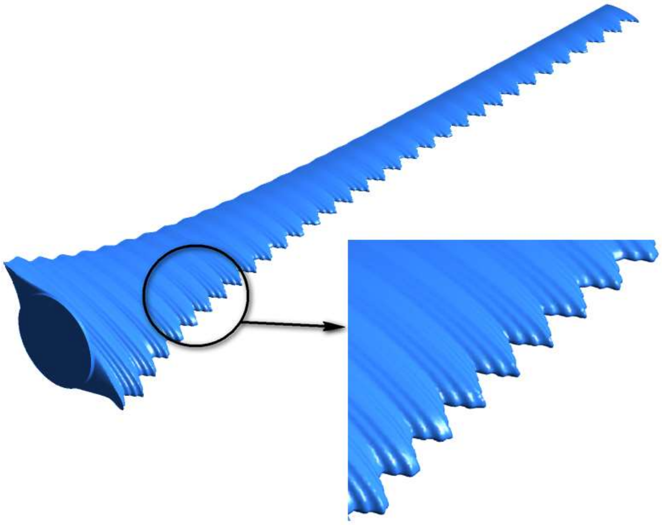

Figure 26: Geometry model- Model-2

### 3.4.2. Boundary Conditions

Due to efforts made to reduce computational time, only one-third of the full domain was modelled with periodic boundary conditions (Velocity distribution at theta equal 0° and 120° are equal), and the blade does not slip. A typical rule of thumb for subsonic flows is that an absolute minimum of 5 characteristic lengths is acceptable. Since the model is full-scale CFD simulations, computational time remained a challenge and to overcome this, a preference to a region of interest was given (in this case downstream is where more accurate turbulence modelling is required). The upstream radius was taken as 2 characteristic lengths of the blade whereas the downstream radius was taken as 5 characteristic lengths of the blade. i.e. an airfoil section with chord c should be modelled in a domain with a minimum radius of 5c. The boundary conditions and domain sizes are shown in Figure 27 and Figure 28.

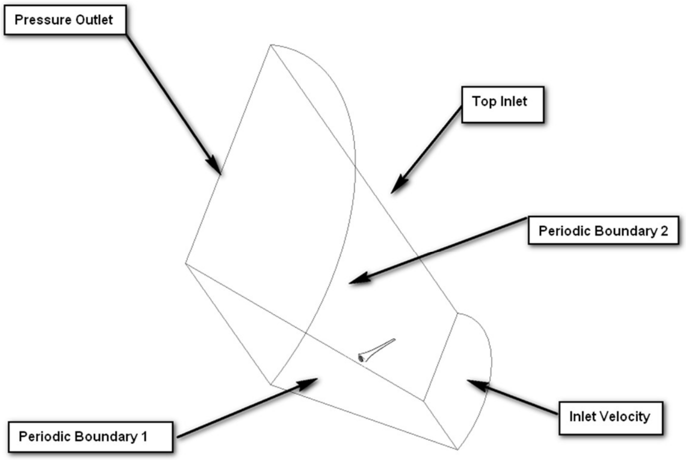

Figure 27: One -Third of the full domain

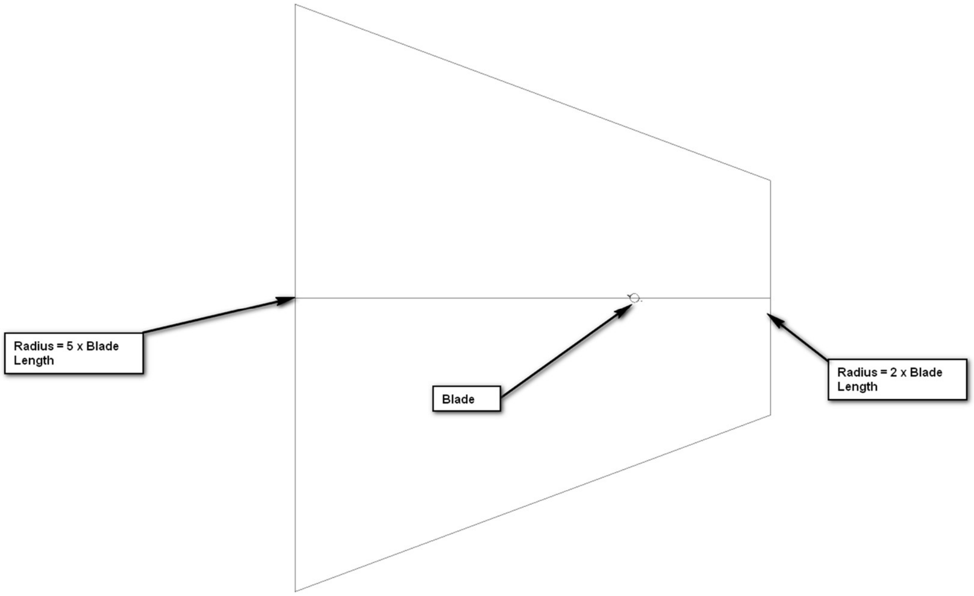

Figure 28: characteristic length with respect to blade length

### 3.4.3. ANSYS Meshing

Quadrilateral unstructured meshing was used; in an unstructured mesh, the orientation of the cell boundaries relative to one another is arbitrary. As a general rule [48] the wall Y-plus should be below 300 to get reasonably accurate results when using the SST turbulence model, and since we are more interested to have accurate predictions of lift, drag, and separation, then Y-plus should be ideally 1 or at least less than 5.

Resolving the viscous sublayer, the first grid cell height was calculated with the following equations,

$$Re_L = \frac{\rho V L}{\mu} \tag{3.4.2}$$

Where,

L = Characteristic length [m]

V = Velocity [m/s]

$\rho$ = Density [kg/m$^3$]

µ = Dynamic Viscosity [kg/ms]

$$Re_L = \frac{\rho V L}{\mu} = \frac{1.225 kg/m^3\ x\, \frac{7m}{s}\ x\ 0.18}{1.8\ x\ 10^{-5} kg/ms}$$

$$Re_L = \ 8.567x\ 10^4$$

$$C_f = 0.058\ (Re_L)^{-2} \tag{3.4.3}$$

$$C_f = 0.058\ (8.567x\ 10^4)^{-0.2}$$

$$C_f = 0.00598$$

$$\tau_\omega = 0.5\ C_f \rho (V)^2 \tag{3.4.4}$$

Where,

$\tau_\omega$ = Wall Shear Stress [kg/ms2]

Cf = Skin Friction Coefficient

ρ = Density [kg/m3]

µ = Dynamic Viscosity [kg/ms]

V = Wind Speed [m/s]

Therefore,

$$\tau_{\omega} = 0.5\ C_f \rho (V)^2 = 0.5\ x 0.00598\ x \frac{1.225 kg}{m^3} x\ (7m/s)^2$$

$$\tau_{\omega} = 0.179 \text{kg/ms2}$$

$$U_{\tau} = \sqrt{\frac{\tau_{\omega}}{\rho}} \tag{3.4.5}$$

Where,

τ$_{\omega}$ = Wall Shear Stress [kg/ms2]

ρ = Density [kg/m3]

$$U_{\tau} = \sqrt{\frac{\tau_{\omega}}{\rho}} = \sqrt{\frac{0.179 \text{kg/ms2}}{1.255 kg/m^3}}$$

$$U_{\tau} = 0.378\ m/s$$

$$Y^{+} = \frac{\rho U_{\tau} Y}{\mu} \tag{3.4.6}$$

Where,

ρ = Density [kg/m3]

μ = Dynamic Viscosity [kg/ms]

$U_{\tau}$= Velocity [m/s]

Y = First Layer height [m]

$Y^{+} \approx 1$

$$Y = \frac{Y^{+} \mu}{U_{\tau} \rho} = \frac{1.8\ x\ 10^{-5} kg/ms}{0.378\ x\ 1.255 kg/m^3}$$

$$Y = 37 x\ 10^{-6} m$$

The first layer height was 20μm. The inflation growth rate was set to 1.1. A low cell growth rate and body of influence were used on the domain to allow a finer mesh in the vicinity of the blade. A finer mesh was required around the blade to accurately capture magnitudes of derived values such as vorticity in the von Karmen vortex sheet which tend to become diluted due to averaging occurring in larger meshes.

One-Third of full domain meshing is shown in *Figure 29*, and Inflation layers for all models are introduced to capture all the boundary effects near the wall of an airfoil,

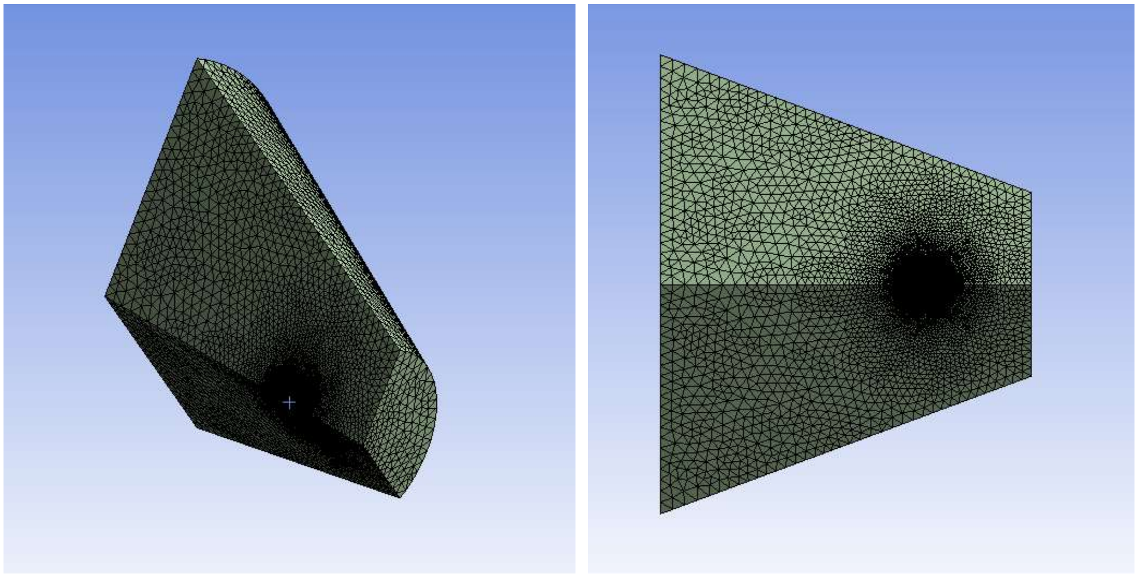

***Figure 29: One-third of the full domain Meshing***

Mesh independence study was conducted; several meshes were refined and tested to make sure that the solution is independent of the mesh resolution. The results are appropriate and within an acceptable range as shown on Table 10 with maximum difference of 5.9%.

**Table 10: Mesh independence result**

| | AOA | Number of Elements | FD | FL | % difference in $_{FD}$ | % difference in $_{Fl}$ |
|---|---|---|---|---|---|---|
| Mesh 1 | 0° | $1.87 \times 10^7$ | 41.5 N | 346.98 N | | |
| Mesh 2 | 0° | $6.972 \times 10^7$ | 43.98 N | 358.44 N | 5.9 | 3.3 |

To improve the mesh quality and to avoid convergence difficulties, Global and local control settings were used i.e. Face sizing, conforming method, body sizing, match control, and inflation. Most importantly the local mesh settings were match control, this is to match the nodes between periodic boundary 1 and periodic boundary 2 to make a 360° visualization in the post-processing stage. As per ANSYS Fluent Tutorial Guide, 2015, The Mesh quality is recommended to be excellent when the skewness spectrum range is between 0- 0.25 (refer to Table *11* and the solution turns to be independent of the grids.

**Table 11:** ***Skewness mesh metric spectrum [48]***

| Excellent | Very Good | Good | Acceptable | Bad | Unacceptable |
|---|---|---|---|---|---|
| 0-0.25 | 0.25-0.5 | 0.5-0.8 | 0.8-0.94 | 0.95-0.97 | 0.98-1 |

Table *12* shows the mesh quality and mesh statistic for the models.

**Table 12:** ***Mesh Statistic and Mesh Quality***

| | Baseline Model | Modified mode 1 | Modified model 4 |
|---|---|---|---|
| Average Skewness | 0.2086 | 0.269 | 0.2029 |

### 3.4.4. ANSYS Solver

The CFD package used is ANSYS FLUENT 19.0. The simulation approach used was moving reference frame (MRF) at an angular velocity of 206.08 RPM. MRF technique is normally used to simulate rotating machinery, the surrounding medium is simulated and the parts remains stationery this is accomplished by adding local accelerations in relation to each grid cell to account for the motion.

The simulation was run under steady-state, pressure-based, Reynolds averaged form of continuity, momentum using SST-k omega turbulence model.

The proposed solver was used because the bio-inspired blade was studied at a low Reynolds number. SST (k-omega) turbulence model was used since flow recirculation or flow separation is the dominant feature in the flow. The fluid used is air at a standard sea-level density of 1.225 kg/m$^3$. Turbulence intensity at the inlet was set to 1.1 % and the turbulence viscosity ratio was 10. Pressure-velocity coupled with gradients were set to least squares cell-based. Pressure, momentum, turbulent kinetic energy and specific dissipation rate equations were solved using the second order-upwind convection scheme. The pseudo transient solution was used to lead to better convergence as the flow is inherently unsteady. Pseudo-time step set to 0.001(s) and convergence residuals were set to $10^{-5}$, However, the solution was only deemed to be converged when CL and CD have converged to a stable value.

# 4. RESULTS

## 4.1. Bio-inspired corrugated airfoils

There were improvements that resulted from optimizing the bio-inspired corrugated airfoil. The major changes that enhanced the performance occurred at the first quarter of the corrugated blade from the leading edge for all. Figure *23* shows the profiles of the optimised shapes with respect to the baseline for max $C_L$, min $C_D$, and max L/D. The changes in the profiles are magnified in the vertical axis and not according to scale in order to better visualize them.

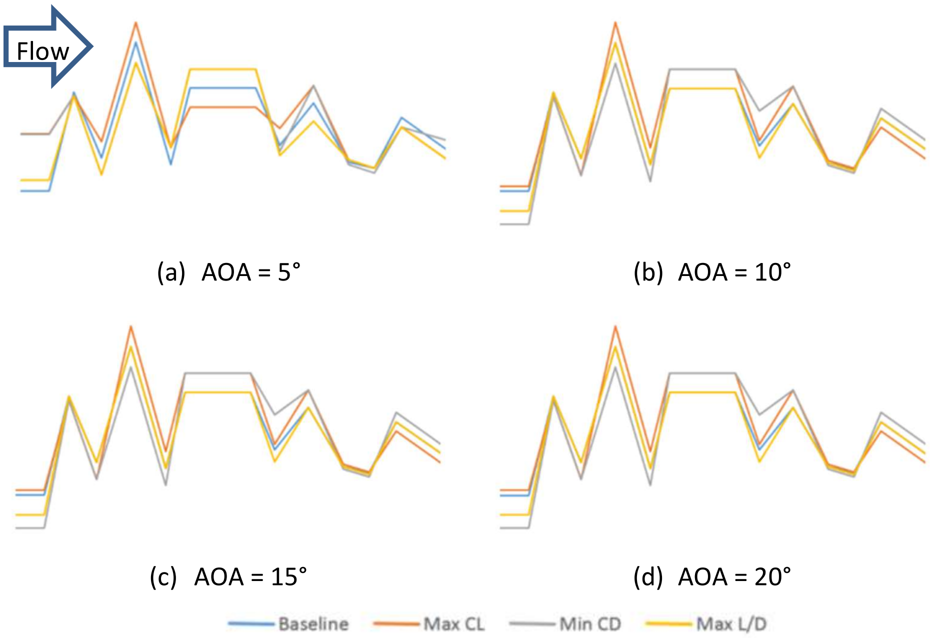

(a) AOA = 5°

(b) AOA = 10°

(c) AOA = 15°

(d) AOA = 20°

**Figure 30: Comparisons of optimised air foil shapes (Diagrams not drawn to scale) with a flow incoming from left to right.**

An interesting observation that can be made apart from AOA = 5°, the Min CD profile for the other airfoils do not necessarily seek to “flatten” out the front section of the airfoil. This is be due to a better attachment of flow to the airfoil thus reducing pressure drag. This is illustrated clearly in Figure 31.

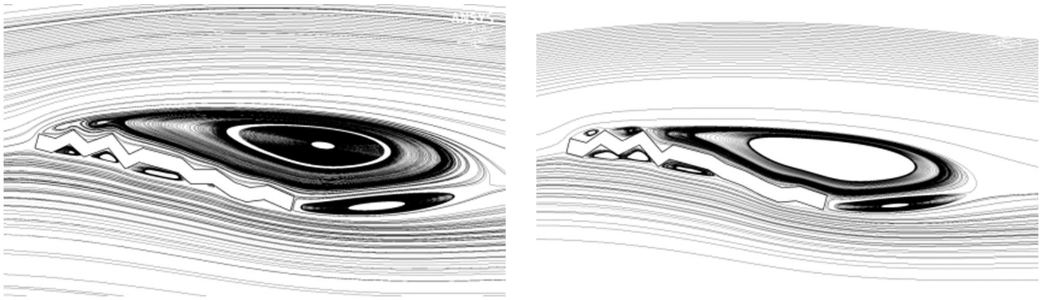

(a) Baseline Geometry (b) Minimum Drag geometry

**Figure 31: Streamlines for AOA 15 comparing baseline with minimum drag optimised profiles**

In terms of the max $C_L$ profiles as depicted in *Figure 30*, one can observe that the second peak is always the highest and the points near the trailing edge are always the lowest thus increasing the overall effective camber of the airfoil. Maximum CL/CD profiles are somewhere in between. The maximum modifications of the nodes for all cases are 22.06% indicating that the assumption to limit the modification of the nodes to 30% was good practice Table 13 compares the optimised coefficients against the baseline values. The largest change in $C_L$ occurs at AOA of 5° with an improvement of 23%, whereas the largest $C_L/C_D$ occurs at AOA 20° with the improvement of 53%. The largest reduction in $C_D$ occurs at AOA of 20° which is 28%.

**Table 13: Comparison of optimised $C_L$, $C_D$ and L/D against the baseline**

| | AOA = 5° | | AOA = 10° | | AOA = 15° | | AOA = 20° | |
|---|---|---|---|---|---|---|---|---|
| | Baseline | Optimised | Baseline | Optimised | Baseline | Optimised | Baseline | Optimised |
| $C_L$ | 0.53 | 0.65 | 0.68 | 0.73 | 0.67 | 0.79 | 0.73 | 0.85 |
| $C_D$ | 0.08 | 0.06 | 0.13 | 0.11 | 0.23 | 0.17 | 0.25 | 0.18 |
| $C_L/C_D$ | 6.95 | 9.24 | 5.17 | 5.68 | 2.88 | 4.17 | 2.90 | 4.43 |

To understand the improvement in lift coefficients of the optimised geometries when compared with the baseline cases, static pressure coefficients over the upper and lower blade surfaces are shown in Figure 32.

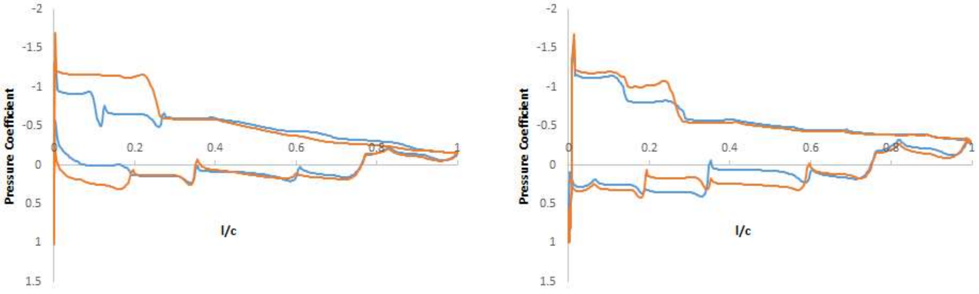

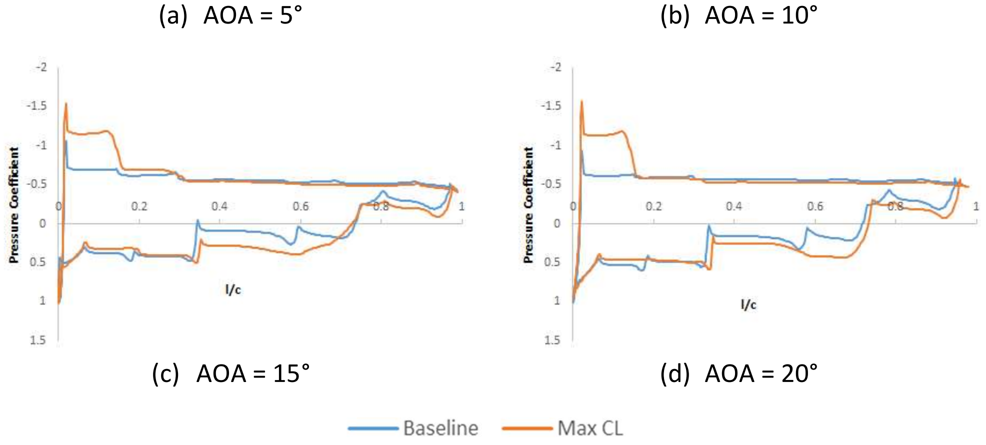
(a) AOA = 5° (b) AOA = 10°

(c) AOA = 15° (d) AOA = 20°

**Figure 32: Static Pressure Coefficients variation along upper and lower blade surfaces for baseline and optimised maximum CL : (a) AOA5°, (b) AOA10°, (c) AOA15° and (d) AOA20°**

From the pressure coefficient plots, one can observe that changes in the geometries extend the low-pressure region near the upper surface leading edge to the upper surface on the second corrugation for AOA = 5° and 10° whereas the baseline geometries have an abrupt drop after the first corrugation. This is not the case for AOA = 15° and 20° where there is a region of low pressure at the first corrugation but drops to the same level as that for the baseline case. The pressure distributions on the lower surface are relatively similar. The similar pressure profile indicates that the baseline shape is already close to the optimal geometry. As the AOA is increased, the airfoil section aft of the first two corrugates plays a more important role in lift generation as evident from the larger difference in $C_P$ between the upper and lower surfaces.

## 4.2. Bio-inspired sinusoidal airfoil

Verification is required for the Post-processing CFD results to confirm the accuracy and reliability, the process of checking the viscous sublayer is important for the accurate prediction of flow separation. As alluded in section 3.4.3 that "Y-plus should be ideally 1 or at least less than 5." And referring to *Table 14*, it is shown that the minimum and maximum are 0.1 and 2.7, respectively. Y-plus is within the speculated range which shows that results are accurate and reliable.

**Table 14: *Wall- Y Plus***

| | Baseline Model | Modified model-1 | Modified model 4 |
|---|---|---|---|

| | | | |
|---|---|---|---|
| Minimum Wall-Y plus | 0.1 | 0.1 | 0.1 |
| Average Wall-Y plus | 1.25 | 1 | 1.25 |
| Maximum Wall-Y plus | 2.7 | 2 | 2.7 |

The velocity at the blade tip should be (hand calculations/analytical results).

$$V = \omega r$$

$$V = -21.58\, rad/s \times 1.95m$$

$$V = 42.081\ m/s$$

Where,

r = blade length 1.95m

ω= angular Velocity -21.58 rad/s

The blade tip velocity for baseline model in CFD-Post processing was found to be approximately between 40m/s to 45m/s. As shown in *Figure 33*, these results are in agreement with the hand calculations shown above.

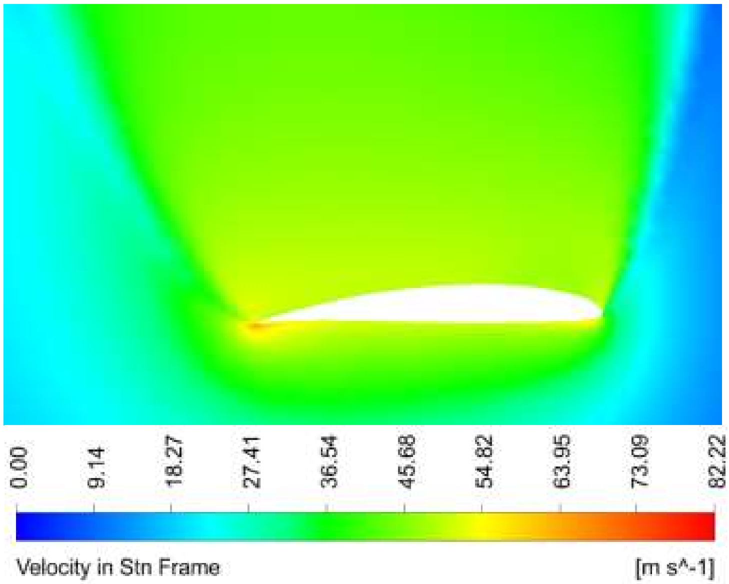

**Figure 33: Blade Velocity**

Total lift and drag forces are directly extracted from Ansys, these forces are calculated by summing up the axis force components. The equations are listed below.

$$L = F_y\,Cos(AOA) \tag{4.2.1}$$

$$D = -F_x\,Cos\,(AOA) \tag{4.2.2}$$

Where,

D = Total Drag Force [N]

L = Total Lift Force [N]

AOA = Angle of Attack [Radians]

$F_y$ = Lift Force component [N]

$F_x$ = Drag Force component [N]

The Angle of Attack is determined by:

$$AOA = \beta - \varphi - \gamma \tag{4.2.3}$$

Where,

$\beta = Flow\ angle$

$\varphi = Twist\ angle$

$\gamma = Pitch\ angle\ (= 0\ for\ this\ case)$

The following method was used to extract the lift and drag coefficients, with the resultant lift and drag forces that are directly extracted from Ansys, the relative velocity is calculated.

Lift and drag coefficient are defined as:

$$C_L = \frac{L}{0.5\rho w^2 l} \tag{4.2.4}$$

$$C_D = \frac{D}{0.5\rho w^2 l} \tag{4.2.5}$$

Where,

L = Lift Force [N]

D = Drag Force [N]

$C_d$ = Coefficient of Drag

$C_L$ = Coefficient of Lift

$\rho$=Density [kg/m$^3$]

$l$ = Blade chord [m]

w = Relative velocity [m/s]

The resultant of the relative velocity is defined as:

$$w = [V^2(1-a)^2 + (\Omega r)^2(1+a')^2]^{0.5} \tag{4.2.6}$$

Where,

w = Relative velocity [m/s]

V = Wind Speed at centre of pressure [m/s]

a = Axial induction factor

$a' =$ Tangential induction factor

$\Omega = Angular\ Velocity\ [\frac{rad}{s}]$

r = Blade length [m]

Power for a single turbine:

$$P = Lz\Omega \tag{4.2.7}$$

Where,

P = Power [w]

L = Lift Force [N],

Z= centre of pressure (Computed by Ansys Fluent)

$\Omega = Angular\ Velocity\ [\frac{rad}{s}]$

**Table 15: Power output for different models**

| | V (m/s) | Cl | Cd | Z (m) | Power (w) | Cp |
|---|---|---|---|---|---|---|
| Baseline Model | 18.13 | 1.66 | 0.217 | 0.84 | 1090.35 | 0.434 |
| Modified model-1 | 18.343 | 1.505 | 0.184 | 0.85 | 1023.9 | 0.408 |
| Modified model 2 | 18.77 | 1.59 | 0.22 | 0.87 | 1168.84 | 0.46 |

The power coefficient is one of the most significant parameters investigated in this study, as stated below

$$T = \frac{P}{\omega} \tag{4.2.8}$$

$$C_p = \frac{2\,T\omega}{\rho A V^3} \tag{4.2.9}$$

The resulting power coefficient of 0.40 from (manual calculations analytical solution) from the formula showed above is compared to power coefficients obtained from the simulation. As shown in *Table 15*, the numerical results coincide with this value, the power coefficient becomes 43.4% compared to the 40% for a baseline model from hand-calculations. The solution matched up quite well considering the fact that there were many assumptions used in the simple 1D momentum theory. The numerical results correctly fall below the Betz limit of 16/27=59.2% for a non-shrouded rotor.

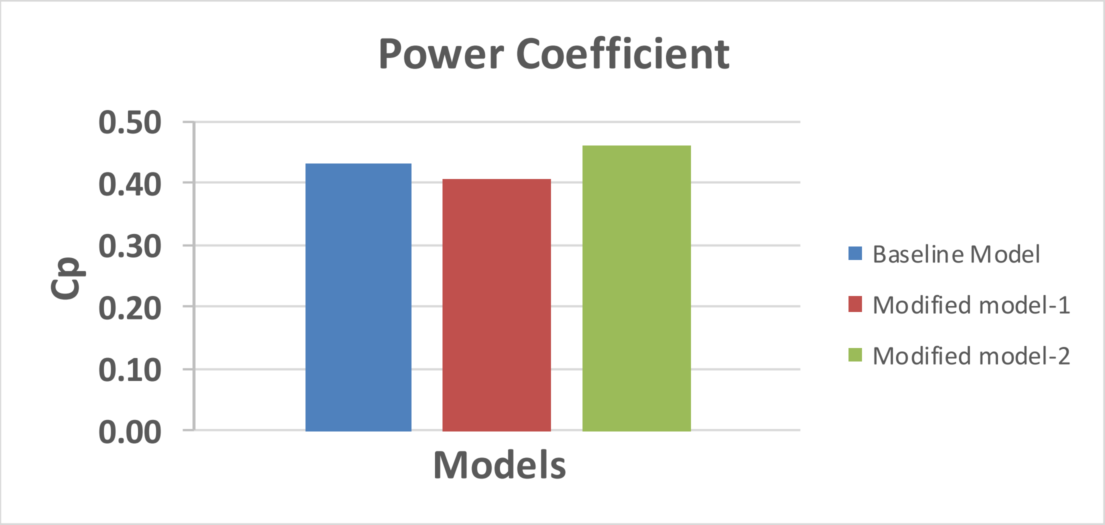

**Figure 34: Power Coefficient comparison**

From the power coefficient comparison shown in *Figure 34* or *Table 15*, the Modified Model-2 has increased its aerodynamic performance by 6% whereas Modified model-1 has decreased by 6% when compared to the baseline model. The centre of pressure and ratio of amplitude to wavelength were the major contributing factors when it comes to increasing or decreasing the aerodynamic performances for modified models. The centre of mass of Modified Model-2 is slightly higher compared to other models which resulted in a higher power coefficient.

As shown in *Figure 35*: Flow features at the root span section -0,5 to -1m in the Z-axis show that baseline and model 1 flow features are comparable whereas for model 2 they are different. Model 2, which is higher in amplitude to wavelength ratio appeared to have altered the flow and resulted in vortex generation at the trough. Model 2 also shows that it has a higher positive pressure at the peaks which results in higher momentum transfer. Although baseline and model 1 are comparable, in some areas baseline seem to have higher positive pressure when compared to model 1, this may have contributed in decreasing the aerodynamic performance of model 1 when compared to baseline since there is low momentum transfer.

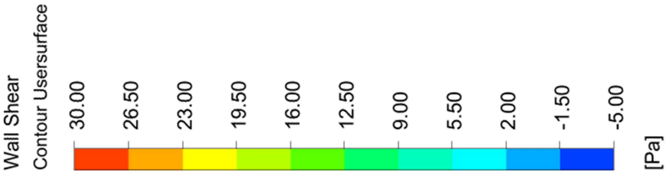

Baseline @ Z-Axis (m) : -0.5 to -1

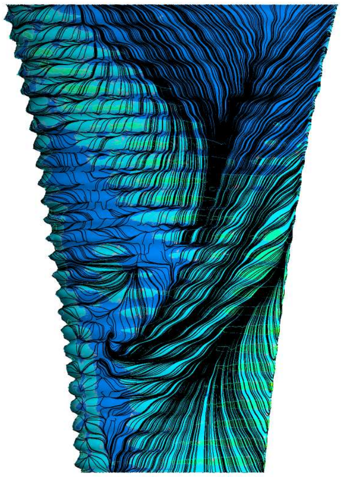

Model 1 @ Z-Axis (m) : -0.5 to -1

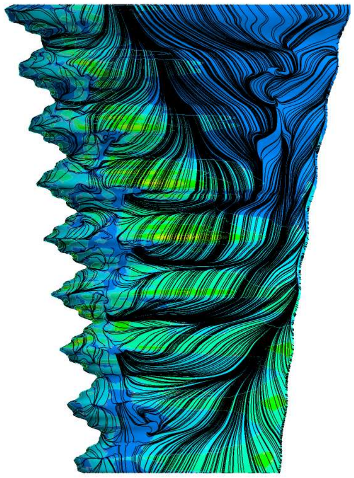

Model 2 @ Z-Axis (m) : -0.5 to -1

Baseline @ Z-Axis (m) : - 1 to -1.5

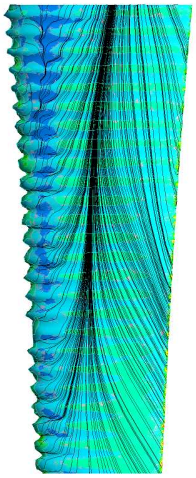

Model 1 @ Z-Axis (m) : - 1 to -1.5

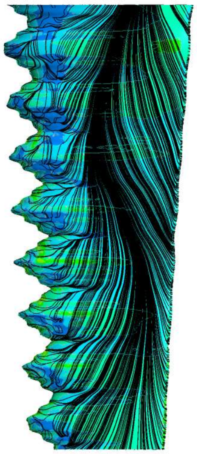

Model 2 @ Z-Axis (m) : - 1 to -1.5

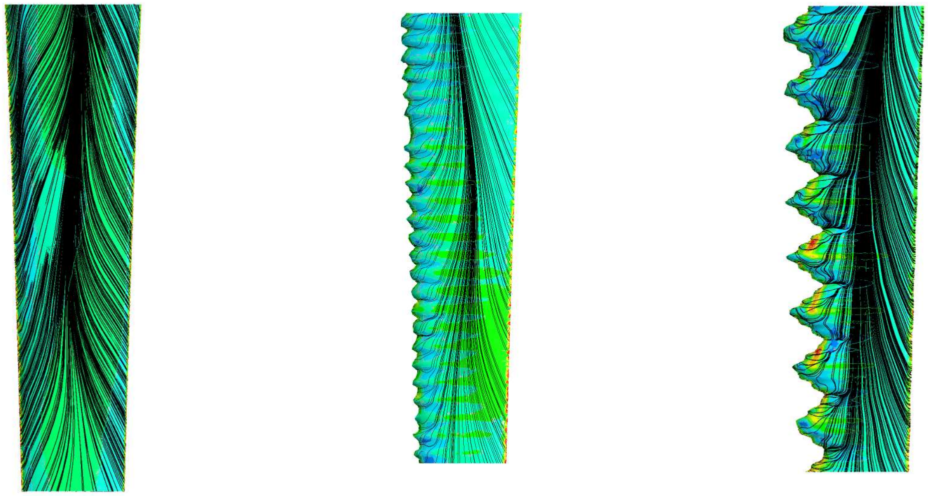

Baseline @ Z-Axis (m) : - 1.5 to -2

Model 1 @ Z-Axis (m) : : - 1.5 to -2

Model 2 @ Z-Axis (m) : - 1.5 to -2

**Figure 35: Wall Shear streamlines**

The flow features for model 1 at the mid-span (-1 to -1.5m Z-axis) differs from baseline model streamlines. Unlike at the root span, where model 1 and 2 show negative pressure at the troughs. Although there is vortex generating for model 1 and 2 at the leading-edge, model 1 remains with lower positive pressure to generate lift.

It is interesting to note that the blade tip, the leading-edge of model 2 has higher positive pressure than any other location on the blade, this location is an optimum point of higher momentum transfer. On the other hand, model 1 has higher positive pressure at the trailing edge, where this results in drag.

The flow patterns for baseline and model 1 are almost similar, and it can be seen there is an attached flow with a spanwise component on a major part of the blade surface near the blade root. The attached flow is a very small area of about 5% of the blade surface at the baseline and model 1. Flow reversal can also be seen as the spanwise flow converges diagonally from the trailing-edge towards the leading-edge. The major difference between baseline and model 1 streamlines is that the converging spanwise for model 1 appears to have dispersed more.

From the mid-span towards the tip of the blade, the spanwise flow starts diverging from the centre of the blade chord. The major difference between baseline and modified blades is that, the diverging spanwise for baseline model and model 2 appears to be denser when compared to model 1 and the attached flow for baseline seems to have extended from the root to the mid span which also causes flow reversals.

The aerodynamic performance of the sinusoidal shape at the leading part of the blade depends on several factors, but most contributing factors are amplitude and wavelength. The presence of the leading-edge tubercles alters the flow around the blade resulting in changes in performance. The comparison between the baseline blade, Model 1 blade and model 2 blade, is shown below, where both modified blades with various amplitudes and wavelengths are compared. These modified blades are also compared to the baseline model.

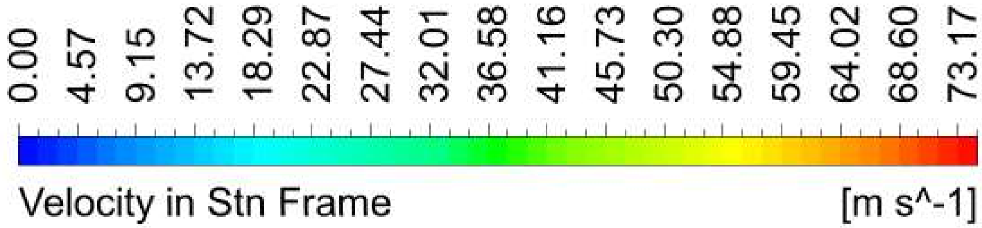

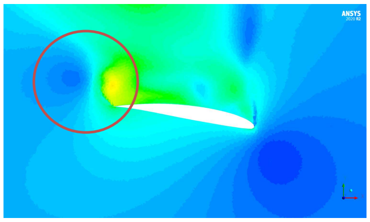
Model 1: Peak- 0.435L span

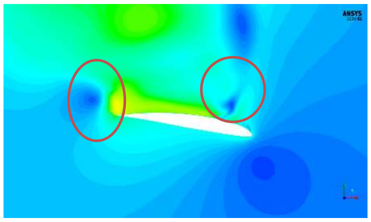
Model 2: Peak- 0.446L span

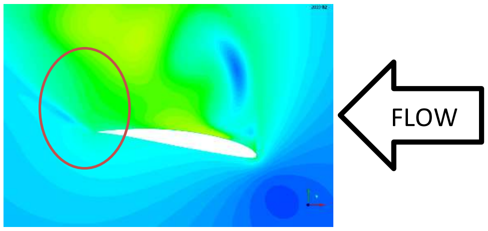

Baseline- 0.435L span

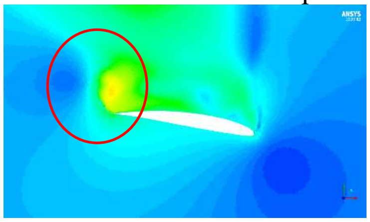
Model 1: Trough- 0.441L span

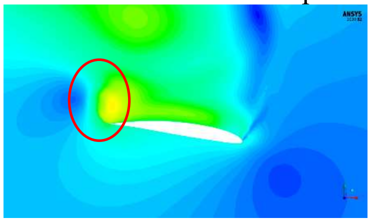
Model 2: Trough- 0.461L span

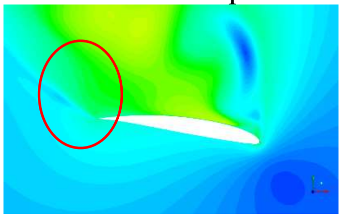
Baseline- 0.441L span

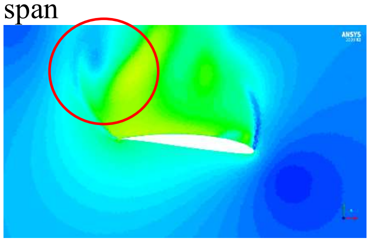
Model 1: Peak- 0.533L span

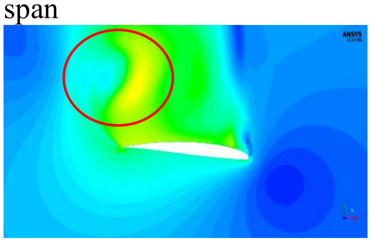
Model 2: Peak-.569L span

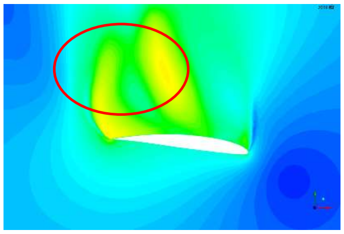
Baseline- 0.533L span

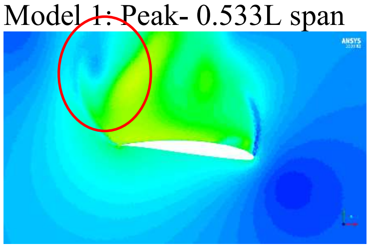
Model 1: Trough- 0.538L

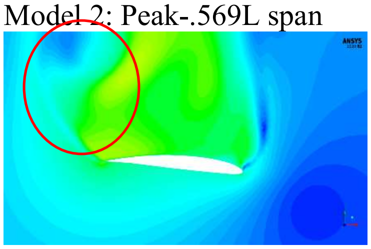
Model 2: Trough- 0.584L

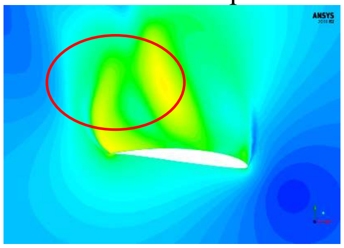
Baseline- 0.538L span

span span

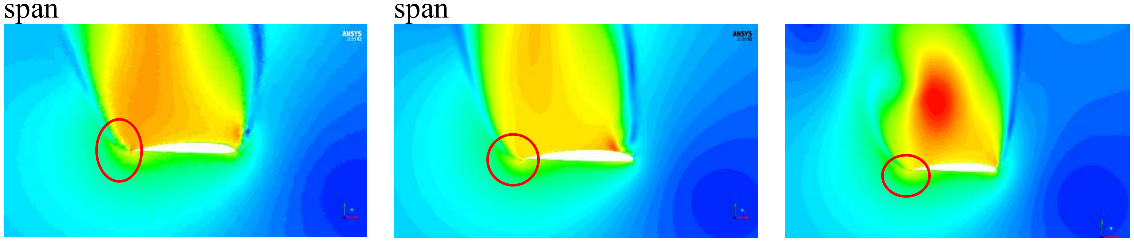

Model 1: Peak- 0.943L span Model 2: Peak- 0.938L span Baseline- 0.943L span

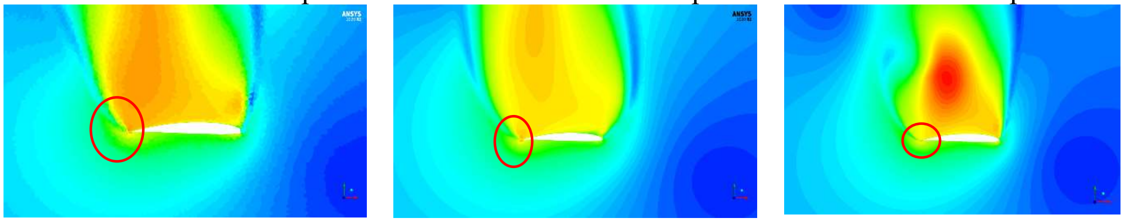

Model 1: Trough- 0.948L span Model 2: Trough- 0.953L span Baseline- 0.948L span

**Figure 36: Velocity Vorticity Field cut-planes for Model 1, model 2 and Baseline**

Vortex generation for modified and baseline models are compared throughout the cut-out planes across the blade span. The trough and the peak of model 2 is not aligned with the trough and the peak of model1, this is because the wavelength of model 2 is 26.1% higher when compared to wavelength of model 1. The cut-out planes were taken from the centre of pressure towards to the tip of the blades.

Model 2 at 0.446L span shows signs of vortex formation in two regions: at the trailing edge and along the middle of the chord (approximately 25% of the chord from the leading edge). These locations are also indicated by red circles. The velocities at these locations are very low and ranges between 0–9 m/s while the surrounding of upper side of the chord ranges between 22-46 m/s , hence they resulted in counter -rotating vortices.

Comparing Model 2 at 0.446L span with Model 1 at 0.435L span from Figure *36*, it is easily noticeable that the two regions where there is vortex formation differs. The difference between these counter-rotating vortices, is that for model-1 counter-rotating vortices appears to have higher vortices when compared to Model-2. On the other hand, the baseline at 850mm from the hub is not showing vortices nor a detachable bubble (see the red circle). It is also observed that model 1 and baseline at 0.441L span, their flow features remained the same as model 1 and baseline 0.435L span whereas for model 2 at 0.461L span, the detachable bubbles that were located at the middle of the chord have moved towards the leading edge. The smaller circulation bubbles as the effect of amplitude to wavelength ratio encourage the transition of the boundary layer from laminar to turbulent flow [23 and 30].It is believed that significant flow separation results in stall-delaying, [36]. Comparing Model 2 at 0.569L span and 0.584L span with Model 1 at 0.533L span and 0.538L span, it can be seen that for model 1, the counter-rotating vortices have detached from the trailing edge and are moving in clockwise direction, whereas for model 2, counter-rotating vortices appears to be weaker ( dissipation signs of vortex generation) than model 1, this is an indication that there is low momentum transfer.

At the tip planes 0.948L span and 0.953L span there are no counter-rotating vortices, only high-volume velocities are formed at the upper side of the blade chord and the velocities overlap to the lower side of the chord at the trailing edge.

Hansen et.al. [50] concluded that the streamwise vortex generation depends on the ratio of amplitude to wavelength, this study is also supported by Rostamzadeh et al. [51] stating that airfoils with higher amplitude to wavelength ratio might generate stronger counter-rotating vortices. The wind tunnel test conducted by Stein and Murray [52] comparing the NACA 0020 profile at Re=250 000 with modified tubercle airfoil confirmed that the performance of conventional baseline was higher than the modified airfoil, however the effects of amplitude to wavelength ratio were never considered.

From the above-mentioned comparison model 1 and model 2, the effects of amplitude to wavelength ratio appeared to have agreed with previous studies.

Figure *37*, shows a comparison done for pressure distribution along the blade. One can observe that the pressure distribution for a baseline blade ranges between -800 to -400 Pa whereas for modified blades the pressure distribution ranges between -3000 to -400 Pa. The pressure profiles for modified blades are similar; however, -3000 Pa is more visible to model 2. It is clearer on Model-2 that the low-pressure region lies closer to the leading edge behind the tubercle troughs as compared to the tubercle peaks.

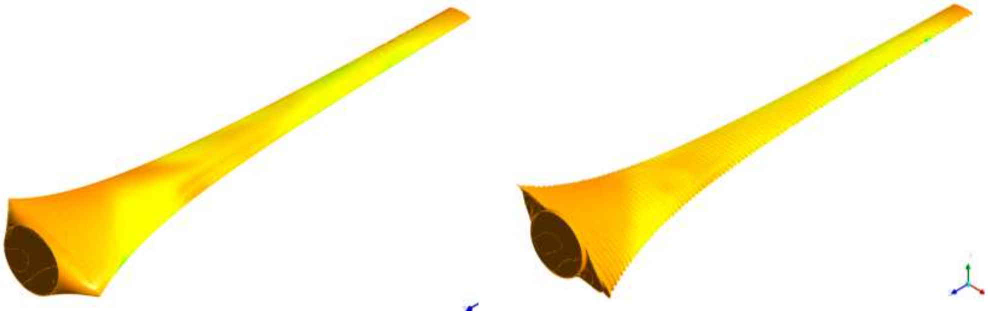

(a) ***Baseline Blade*** (b) ***Modified Model 1 Blade***

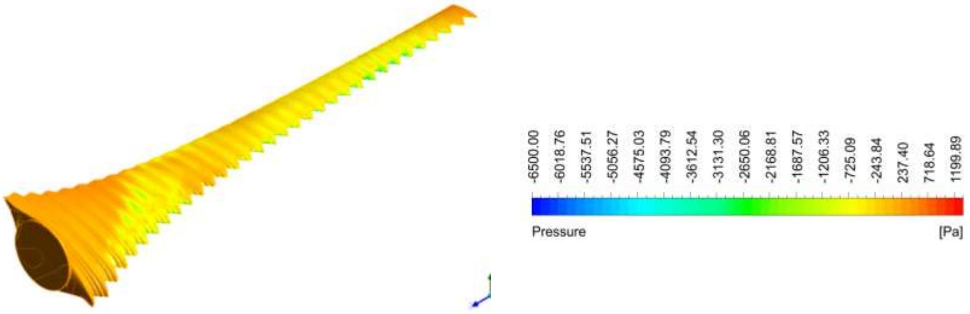

(c) ***Modified Model 2 Blade*** (d) ***Legend***

**Figure 37: Pressure Contour**

To understand the pressure distribution between the baseline model and modified models, a comparison is done using the pressure plot field cut-planes as shown from Figure *38* to Figure 43. Figure *38* behaves similarly Figure *39* to except that in Figure *39*, modified models are now comparable at the leading edge and at 25% from the leading edge. Figure *40* and Figure *41* at the midpoint of the blade behaves differently from Figure *38* and Figure *39*. The distinction is seen clearly because for Figure *40* and Figure *41* the baseline model at the trailing edge has the lowest pressure of approximately -1400Pa compared to its relative modified models, whereas the pressure for Figure *38* and Figure *39* is increasing significantly towards the trailing edge at a pressure of approximately -200 Pa. At the tip planes, Figure *42* and Figure *43* behave similarly to Figure *40* and Figure *41*, except that for Figure *42*, model 1 at the 50% from leading edge is 250Pa whereas baseline and model 2 are comparable with 1000Pa.

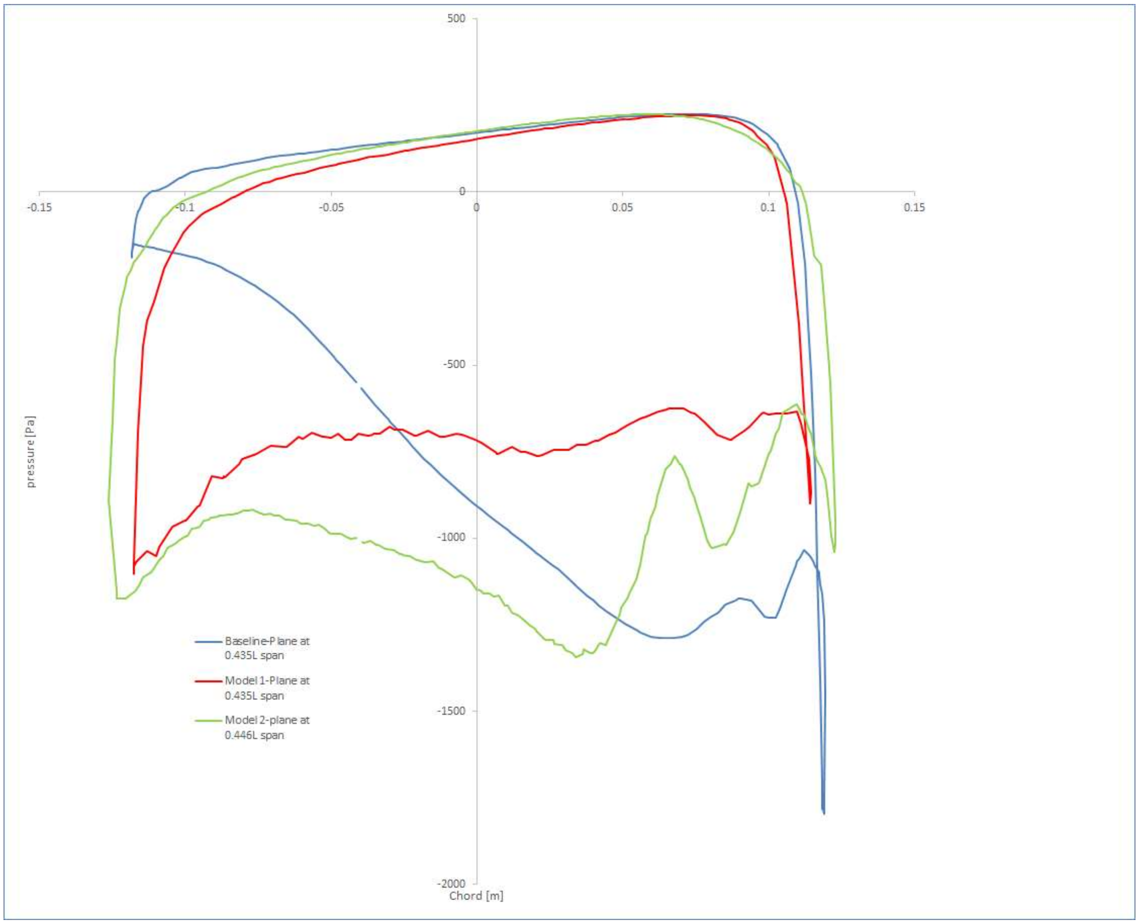

**Figure 38: Pressure plot Field cut planes for Model 1, model 2 and Baseline.**

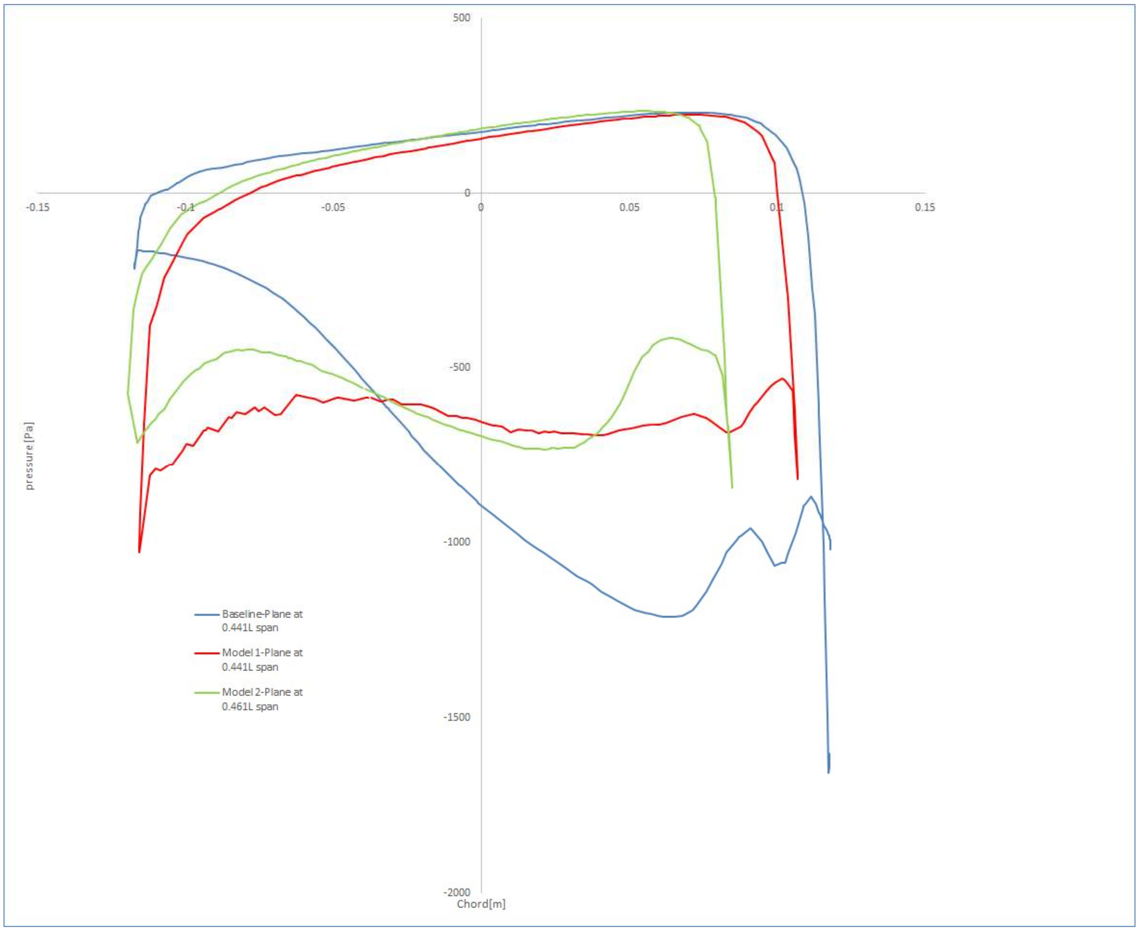

**Figure 39: Pressure plot Field cut planes for Model 1, model 2 and Baseline.**

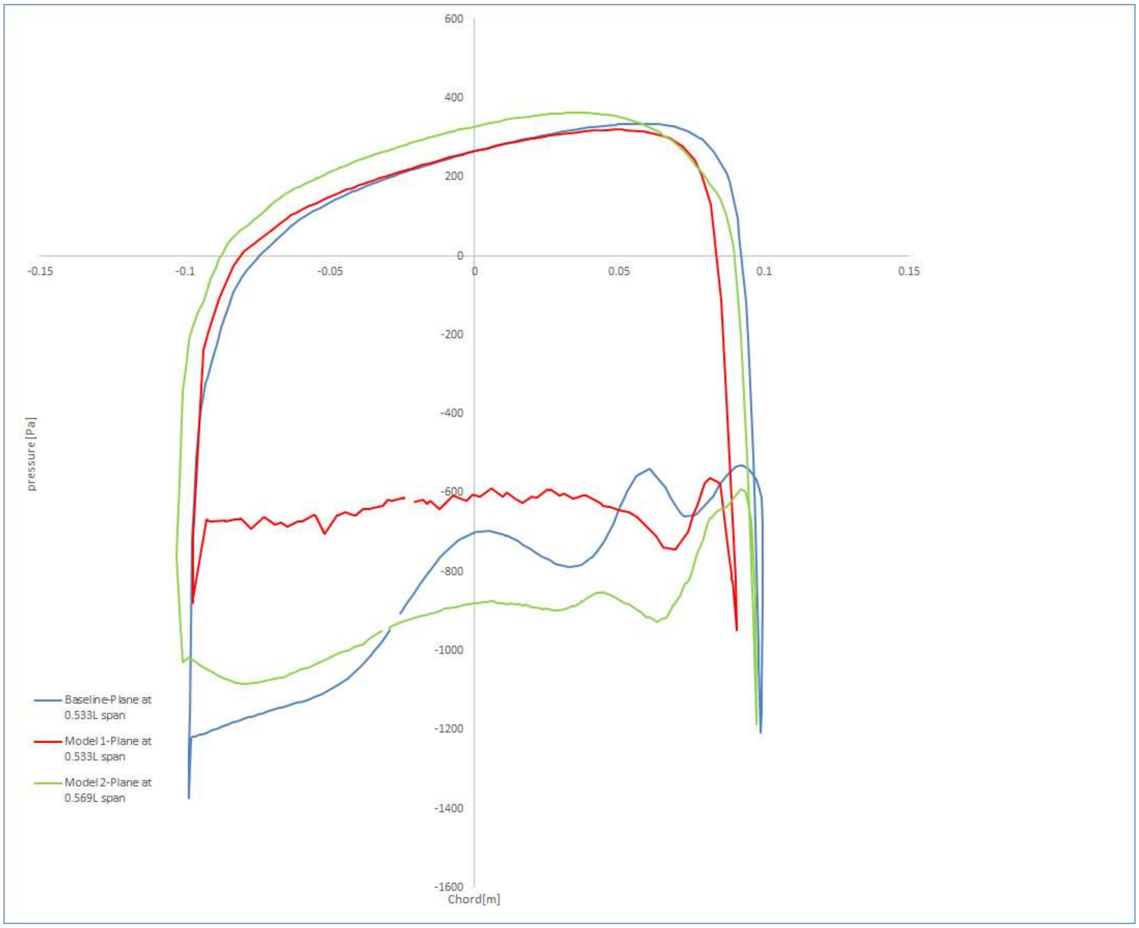

**Figure 40: Pressure plot Field cut planes for Model 1, model 2 and Baseline.**

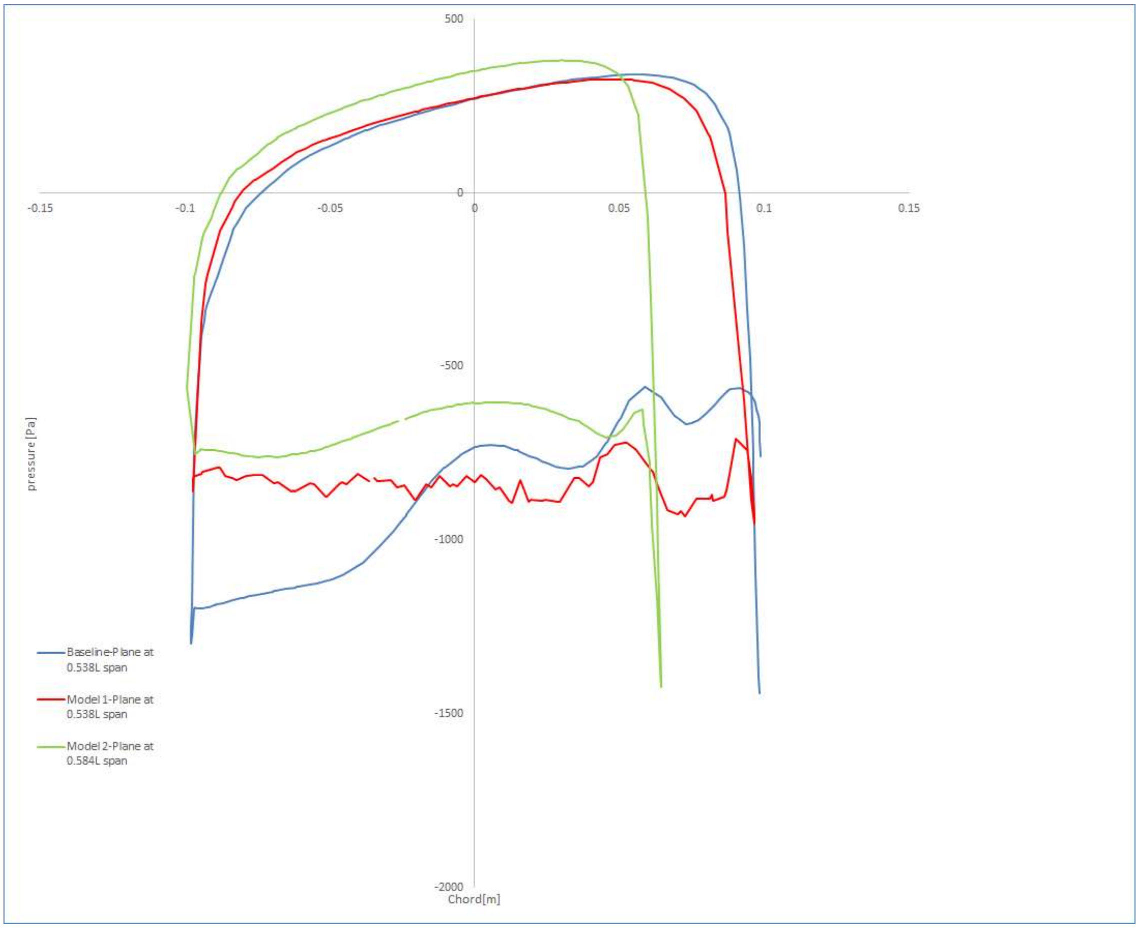

**Figure 41: Pressure plot Field cut planes for Model 1, model 2 and Baseline.**

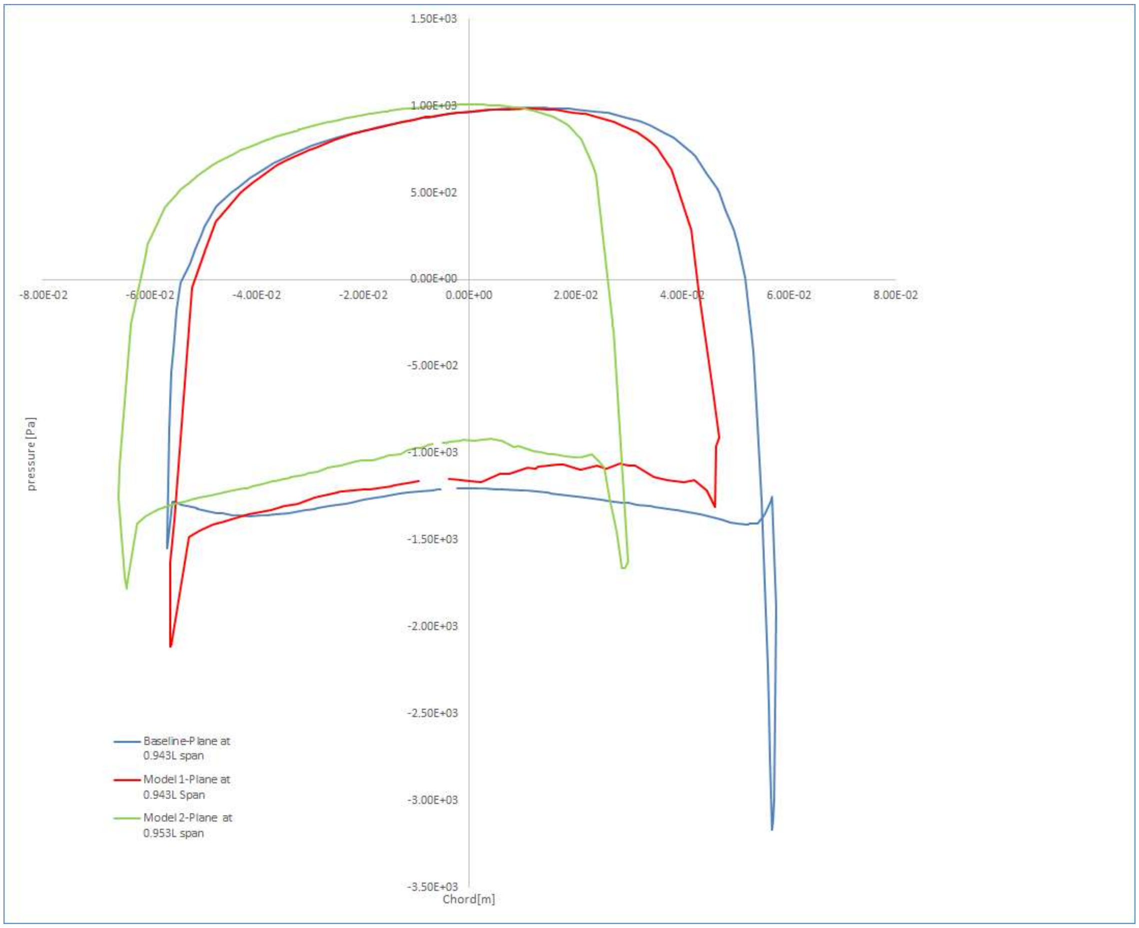

**Figure 42: Pressure plot Field cut planes for Model 1, model 2 and Baseline.**

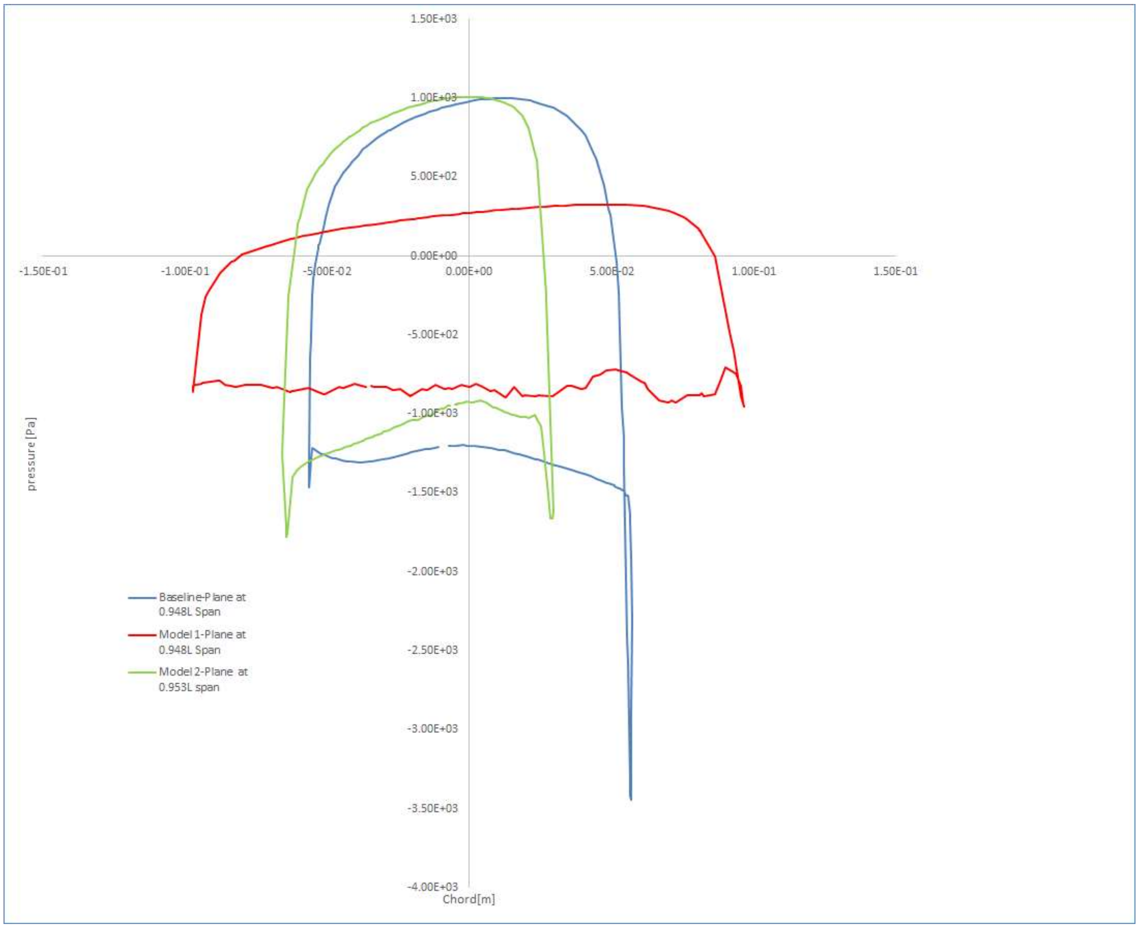

**Figure 43: Pressure plot Field cut planes for Model 1, model 2 and Baseline.**

# 5. CONCLUSION AND DISCUSSIONS

## 5.1. Introduction

In this study the main objections were to investigate and develop a comprehensive understanding of aerodynamic characteristics of an airfoil with different wavelength and amplitude at the leading-edge at low Reynolds numbers, and to optimize the geometry of corrugated airfoil at the different angles of attack (AOA) ranging from 5° to 20° at chord Reynolds number $Re = 9.89 \times 10^3$ which corresponding to 2.799 m/s wind velocity at a chord length of 50.25 mm.

The effects of optimising corrugated airfoil, lift and drag performance, and flow behaviour on corrugated airfoil and sinusoidal shape has been investigated. 2D simulation was done to optimize the shape of Bio-inspired corrugated airfoils whereas 3D simulation was used for Bio-inspired sinusoidal airfoils. The simulations were done using Ansys fluent 19.0 CFD software, whereby it was verified ( Knudsen number is below 30%) that accurate and reliable results were obtained. In preparation for the solver, the Mesh independence study conducted confirmed to be acceptable since all cells are independent and will never affect the solution.

## 5.2. Bio-inspired corrugated airfoil shapes for wind turbine blades

An optimization exercise based on a baseline corrugated airfoil taken from previous studies has been conducted in Ansys Fluent using the Workbench Design Explorer tool. From the results we can conclude that the geometry used in the previous studies can be further optimised and the major changes that enhanced the performance occurred at the first quarter of the corrugated blade from the leading edge particularly around the first two corrugations. This is due to the transition taking place at the boundary layer from laminar to turbulent flow. The peak of a corrugated airfoil acts as a tabulator to generate unsteady vortex structures to promote the transition of the boundary layer. There is enough momentum convection at the first two peaks that tends to provide enough kinetic energy within the boundary layer to overcome the adverse pressure gradient.

Significant improvements in CL, CD and L/D were achieved through this optimization exercise. Interestingly, the optimised geometries for drag reduction are not always "flatter" than the baseline. The effects of the optimised corrugations reduced the separation region thus reducing drag even though the overall thickness increased marginally.

### 5.3. Bio-inspired sinusoidal air-foil shapes for blades

An exercise to compare the aerodynamics effects at the sinusoidal leading-edge of the blade was conducted using CFD Ansys fluent 19.0. The effects of SG6042 modified blades are compared with baseline blades and significant improvements were contributed by tapered geometry and the effects of wavelength and amplitude.

The tapered geometry for modified model 2 has a higher centre of pressure when compared to modified model 1 and the baseline model. This has resulted model 2 having a higher coefficient of power. As depicted in section 4.2., the model 2 (with higher wavelength and higher amplitude) appeared to have a higher power coefficient when compared to SG6042 model 1 and baseline.

An interesting observation was noted when results from Table 15 indicated that there is a significant decrease of $C_d$ of model 1 by 15.2% whereas $C_d$ of model 2 has increased by 1.4% when compared to the baseline model. Although model 1 shown Cd improvements, its respective $C_L$ was reduced by 9.34% whereas model 2 is reduced by 4.2%.

The flow pattern has revealed that the tubercles at the leading-edge of the blade does assist in altering the flow and results in vortex generation. The higher positive pressure at the peaks and lower negative pressure at the trough increased the momentum transfer, this has favoured model 2, since it has higher amplitude and wavelength. Although there is vortex generating for model 1 and 2 at the leading-edge that resulted in delaying stall, model 1 remains with lower positive pressure to generate lift.

It is observed that there is a direct correlation between wavelength, amplitude, and the tapered geometry which has led to the aerodynamic performance of SG6042 model 2 considered to be suitable for the small-scale horizontal wind turbine.

## 6. FUTURE WORK

As to improve the accuracy of these results, future work should focus on optimised shaped blades conducted in 2D at different AOA and shall be blended to 3D turbine for small horizontal axial wind turbines. The investigation shall compare optimised blended 3D and conventional turbines.

The investigations with and without tapered or twisted of the blade shall be studied. Comparison of the blade with and without tapered or twisted is still required to determine the effects of sinusoidal at the leading-edge of the blade.

# REFERENCES

1. Cheremisinoff, N.P, *Fundamental of Wind Energy*, Ann Arbor science, 1978.
2. The South African Energy sector report, 2019
3. Panwar, N.L., Kaushik, S.C., and Kothari, S., *Role of renewable energy sources in environment protection: A review,* Renewable, and Sustainable Energy Reviews, 2011, (15): 1513–1524
4. Karekezi, S., Kithyoma, W. Renewable energy in Africa prospers and limits, 2003
5. Energy information administration, international outlook, 2017
6. https://en.wikipedia.org/wiki/Medupi_Power_Station [Accessed 2020]
7. https://en.wikipedia.org/wiki/Kusile_Power_Station [Accessed 2020]
8. https://www.engineeringnews.co.za/article/nxuba-wind-farm-starts-generation-delivery-of-energy-2020-26#:~:text=The%20Nxuba%20Wind%20Farm%20is, GWh%2Fy%20to%20the%20grid. [Accessed 2020]
9. Manwell, J. F., McGowan, J. and Rogers, A. *Wind power explained: theory, design and application*, second edition, 2009, Chichester, UK: Wiley.
10. Hansen, M.O.L., *Aerodynamics of Wind Turbines*, second edition, 2008, Earthscan.
11. Dixon, S. L., and Hall, C.A., *Fluid mechanics and Thermodynamics of turbomachinery*, six edition, 2010, Butterworth-Heinemann is an imprint of Elsevier.
12. EL-BAZ, A.R., Youssef, K. and Abdel-Maksoud, M. *Improving the performance of Savoius wind turbine using three-rotors design,* Proceedings of ICFD11: Eleventh international conference of fluid Dynamics December 19-23, 2013, Alexandria, Egypt.
13. Kruger, A.C., Goliger, A.M., Retief, J.V, and Sekele, S. Strong Wind Climatic Zones in South Africa. *Wind and Structures*, Volume 13(1), 2010
14. South Africa National Standards, SANS 10400 Part XA: Energy usage in Buildings, 2011 edition 1.
15. http://www.vortexfdc.com/markets/wind-and-site.html [ Accessed 2015]
16. Joshi, S.N. and Gujarathi, Y.S., *A Review on Active and Passive Flow Control Techniques,* International Journal on Recent Technologies in Mechanical and Electrical Engineering (IJRMEE), Volume :3 issue:4
17. Giguere, P. and Selig, M.S., *New air foils for small horizontal axis wind turbine,* Journal of solar energy engineering, volume 120, 1998:108-114.
18. Giguere, P. and Selig, M.S., *Low Reynolds Number Airfoils for Small Horizontal Axis Wind turbines,* Wind engineering, volume 21(6), 1997:367-380.
19. https://en.wikipedia.org/wiki/Bumblebee#/media/File:Bumblebee_October_2007-3a.jpg [ Accessed 2020]

20. https://en.wikipedia.org/wiki/Dragonfly#/media/File:PantalaFlavescensTalakaveri.jpg [ Accessed 2020]
21. Till, D.,Wanke, S., Et Al. *Modelling and Manufacturing of dragonfly wing as basis for bionic research*, international design conference, 15, pp.18,2006.
22. Azuma, A., Azuma, S., Watanabe, I. Furuta, T., Flight mechanics of a dragonfly, Journal of experimental biology, volume 116, 1985, 79-107.
23. Hu, H. and Tamai, M. *Bioinspired Corrugated Air foil at Low Reynolds Numbers*, Journal of Aircraft, 2008, 45(6).
24. New, T.H., Chan, Y.X., and Koh, G.C. *Effects of corrugated air foil surface features on a flow-separation control*, AAIA Journal, 2014, 52(1).
25. Kesel, A.B. *Aerodynamic characteristic of dragonfly wing sections compared with technical airfoil*, the journal of experimental Biology volume 203, 2000: 3125-3135.
26. Vargas, A. and Mittal, R. *Aerodynamic Performance of Biological Airfoils*, 2nd Flow Control Conference, 2004.
27. Rees, C. *Aerodynamic properties of an insect wing section and a smooth airfoil compared*, Nature, Volume 258, 1975, 141-142.
28. Rees, C. *Form, and function in corrugated insect wings,* Nature, Volume 256, 1975: 200-203.
29. Newman, B.G., Savage, S.B., and Schouella, D. *Model Test on a Wing Section of an Aeshna Dragon, Scale Effects in Animal Locomotion*, London, Academic Press, 1977: 445-477.
30. Murphy, J. and Hu, H. *An experimental investigation on a bio-inspired corrugated air foil*, Exp Fluids, 2010, 49: 531-546.
31. Ho, W.H. and New, N.T. CFD analysis of bio-inspired corrugated airfoils. Proceedings of ICFD11: Eleventh International Conference of Fluid Dynamics, Egypt
32. Ho, W.H. and New, N.T. *Unsteady numerical investigation of two different corrugated air foils*, Proceedings of the Institute of Mechanical Engineering Part G: Journal of Aerospace Engineering, 2016.
33. Premachanda, S., Giacobello, M., *The Effect of Wing Corrugations on Aerodynamics Performance of Low-Reynolds Number Flapping Flight*. 17th Australasian Fluid Mechanics Conference, 2010.
34. Majumdar, K. An investigation into the vortex formation in a turbulent fluid with an application in tropical storm generation, arXiv preprint nlin/0310045,2003.
35. Yarusevych, S., Sullivan, P. E., Kawall. J.G., On *Vortex Shedding from an air foil in low-Reynolds- numbers flow*, *Journal of Fluid Mechanics,* Volume 632, *2009,* 245-271.

36. Fish, F. E., & Battle, J. M. *Hydrodynamic design of the humpback whale flipper.* Journal of Morphology, Volume 225, Issue 1, 1995: 51-60.

37. Fish, F.E., Weber, P.W. Murray, M.M., and Howle, L.E. The Tubercles on Humpback Whales' Flippers: Application of Bio-Inspired Technology, *Integrative and Comparative Biology, 2011, 51(1):203-213*
38. Miklosovic, D.S., Murray, L.E., and Fish, F.E., Leading-edge tubercles delay stall on humpback whale (Megaptera novaeangliae) flippers, *Physics of Fluids*, 2004(16,5): L39-L42
39. Bai, C.J., Wang, W.C., and Chen, PW. The effects of sinusoidal leading edge of turbine blades on the power coefficient of horizontal-axis wind turbine (HAWT), *International Journal of Green Energy,* 2016,13(12):1193-1200
40. Bolzon. M. D.P., Kelso, R. M., Arjomandi. M., Formation *of vortices on a tubercled wing, and their effects on drag,* Aerospace Science and Technology 56 (2016) 46–55
41. Zhang, R.-K., and Wu, J.-Z. Aerodynamic characteristics of wind turbine blades with a sinusoidal leading edge, *Wind Energy, 2012(15):407-424*
42. Goruney. T., Rockwell. D., Flow past a delta wing with a sinusoidal leading edge: near-surface topology and flow structure. Exp Fluids, 2009, 47:321–331
43. Bushnell, D.M., and Moore, K.J. Drag reduction in nature, *IN: Annual review of fluid mechanics*, 1991(23):65-79
44. Sethian, J.A., *Computational fluid dynamics. In: From Desktop to Teraflop: Exploiting the US Lead in High Performance Computin*g. NSF Publications, National Science Foundation, Washington, DC, USA, 1993.
45. Xia, B., and Sun, D.-W. Application of computational fluid dynamics (CFD) in the food industry: a review, *Computer, and Electronics in Agriculture, Volume* 34, 2002:5-24.
46. *Paton, R.T., Computational Fluid Dynamics Companion MECN4021-Fluids Dynamics,* Wits University school of mechanical, industrial & Aeronautical Engineering, 2016.
47. Ali, M.S.M., Doolan, C.J. and Wheatley, V. *Grid convergence study for a two-dimensional simulation of flow around a square cylinder at a low Reynolds number*, Seventh International Conference on CFD in the Minerals and Process Industries, 2009.
48. ANSYS Fluent Tutorial Guide.
49. Kreith, F., Berger, S.A., and et.al." *Fluid Mechanics" Mechanical Engineering Handbook, Boca Raton: CRC LLC, 1999*

50. Hansen, K. L., Kelso, R. M., & Dally, B. B. *Performance variations of leading-edge tubercles for distinct airfoil profiles.* AIAA Journal, Volume 49, Issue 1, 2011: 185-194.

51. Rostamzadeh, N., Hansen, K. L., Kelso, R. M., & Dally, B. B. *The formation mechanism and impact of streamwise vortices on NACA 0021 airfoil's performance with undulating leading edge modification.* Physics of Fluids, 2014: 26(10), 107101.
52. Stein B. and Murray M. M. *"Stall mechanism analysis of humpback whale flipper models,"* Proceedings of Unmanned Untethered Submersible Technology (UUST), Durham, NH, August 2005.

## Appendix A: Parametric Expressions

Gridline C shows vertical/horizontal upper limits of the blade whereas Gridline G and shows vertical/horizontal lower limits of the blade. Both the upper limits and lower limits have the flexibility to populate design points automatically withing a given 30% of a maximum upper bound and minimum lower bound. To maintain the constant thickness throughout the generation of design point, the lower points of the blade are linked to upper points. The parameter equation is expressed similarly to the equations below,

Gridline L & 7 $Parametric\ expression = \min\left(\max(F7, Pv1)\right., E7$

Gridline L &22 $Parametric\ expression = \min\left(\max(F22, Ph2)\right., E22$

Where,

The redefined parametric expression value always remains between gridline F7 and E7 or F22 and E22.

Pv = Vertical points,

Ph = Horizontal points,

T = Blade thickness (mm)

| Gridlines | | C | D | E | F | G | H | I | J | K | L | M | N | O | |
|---|---|---|---|---|---|---|---|---|---|---|---|---|---|---|---|
| Gridlines | | Upper limits | | 0.3 | 0.3 | Lower Limits (mm) | | Thickness (mm) | 0.3 | 0.3 | Upper limits | | Lower limits | | |
| | | Vertical with respect to reference | | Max Upper Bounds | Min Lower Bounds | Vertical with respect to reference line | | Vertical | Max Upper Bounds | Min Lower Bounds | Parametric Expression | | Parametric Expression | | Distance to nearest node (mm) |
| 5.0 | | | $P_v$ | | | | $P_v$ | t | | | | | | | |
| 6.0 | | | | | | | | | | | | | | | |
| 7.0 | | V1 | 14.1 | 14.6 | 13.6 | V2 | 11.4 | 2.7 | 11.9 | 10.8 | =min(max(F7, Pv1), E7 | | =Pv1- t | | 1.8 |
| 8.0 | | V3 | 15.9 | 16.5 | 15.4 | V4 | 12.8 | 3.1 | 13.4 | 12.3 | =min(max(F8, Pv3), E8 | | =Pv3- t | | 1.8 |
| 9.0 | | V5 | 13.8 | 14.5 | 13.2 | V6 | 11.3 | 2.6 | 11.9 | 10.6 | =min(max(F9, Pv5), E9 | | =Pv5- t | | 2.1 |
| 10.0 | | V7 | 16.4 | 17.2 | 15.7 | V8 | 13.9 | 2.6 | 14.7 | 13.1 | =min(max(F10,Pv7), E10 | | =Pv7- t | | 2.6 |
| 11.0 | | V9 | 13.3 | 13.9 | 12.8 | V10 | 10.9 | 2.4 | 11.4 | 10.4 | =min(max(F11,Pv7), E11 | | =Pv9- t | | 1.8 |
| 12.0 | | V11 | 15.1 | 15.7 | 14.6 | V12 | 13.2 | 1.9 | 13.8 | 12.7 | =min(max(F12,Pv11), E12 | | =Pv11- t | | 1.8 |
| 13.0 | | V13 | 13.3 | 13.7 | 12.9 | V14 | 11.1 | 2.2 | 11.5 | 10.7 | =min(max(F13,Pv13), E13 | | =Pv13- t | | 1.4 |
| 14.0 | | V15 | 14.8 | 15.2 | 14.3 | V16 | 12.6 | 2.2 | 13.0 | 12.2 | =min(max(F14,Pv15), E14 | | =Pv15- t | | 1.4 |
| 15.0 | | V17 | 13.3 | 13.4 | 13.2 | V18 | 11.2 | 2.1 | 11.2 | 11.1 | =min(max(F15,Pv17), E15 | | =Pv17- t | | 0.2 |
| 16.0 | | V19 | 13.1 | 13.2 | 13.0 | V20 | 10.9 | 2.2 | 11.0 | 10.9 | =min(max(F16,Pv19, E16 | | =Pv19- t | | 0.2 |
| 17.0 | | V21 | 14.3 | 14.6 | 13.9 | V22 | 12.3 | 2.0 | 12.6 | 11.9 | =min(max(F17,Pv21`, E17 | | =Pv21- t | | 1.2 |
| 18.0 | | V23 | 13.3 | 13.6 | 13.0 | V24 | 11.5 | 1.8 | 11.8 | 11.2 | =min(max(F18,Pv23`, E18 | | =Pv23- t | | 1.0 |
| 19.0 | | Upper limits | | 0.3 | 0.3 | Lower Limits (mm) | | Thickness (mm) | 0.3 | 0.3 | Upper limits | | Lower limits | | |
| 20.0 | | Horizontal with respect to reference | | Max Upper Bounds | Min Lower Bounds | Horizontal with respect to reference line | | Vertical | Max Upper Bounds | Min Lower Bounds | Parametric Expression | | Parametric Expression | | Distance to nearest node (mm) |
| 21.0 | | | Ph | | | | | t | | | | | | | |
| 22.0 | | H2 | 11.2 | 12.1 | 10.3 | H3 | 12.0 | 0.8 | 12.9 | 11.1 | =min(max(F22,Ph2), E22 | | =Ph2+ t | | 3.0 |
| 23.0 | | H4 | 14.2 | 15.1 | 13.3 | H5 | 14.1 | -0.1 | 15.0 | 13.2 | =min(max(F23,Ph4), E23 | | Over-Constrain | | 3.0 |
| 24.0 | | H6 | 17.4 | 18.4 | 16.5 | H7 | 18.0 | 0.5 | 18.9 | 17.0 | =min(max(F23,Ph6), E24 | | Over-Constrain | | 3.2 |
| 25.0 | | H8 | 25.1 | 26.0 | 24.2 | H9 | 25.5 | 0.4 | 26.4 | 24.6 | =min(max(F23,Ph8), E25 | | Over-Constrain | | 2.9 |
| 26.0 | | H10 | 35.7 | 36.6 | 34.9 | H11 | 35.5 | -0.2 | 36.4 | 34.7 | =min(max(F23,Ph10), E26 | | =Ph10- t | | 2.8 |
| 27.0 | | H12 | 42.5 | 43.8 | 41.3 | H13 | 42.9 | 0.3 | 44.1 | 41.6 | =min(max(F23,Ph12), E27 | | Over-Constrain | | 4.1 |
| 28.0 | | H14 | 46.6 | 47.6 | 45.7 | H15 | 47.0 | 0.3 | 47.9 | 46.0 | =min(max(F23,Ph14), E28 | | Over-Constrain | | 3.1 |
| 29.0 | | H16 | 49.7 | 50.7 | 48.8 | H17 | 50.4 | 0.7 | 51.3 | 49.5 | =min(max(F23,Ph16), E29 | | Over-Constrain | | 3.1 |
| 30.0 | | H18 | 58.3 | 60.0 | 56.7 | H19 | 58.2 | -0.1 | 59.8 | 56.6 | =min(max(F23,Ph18), E30 | | Over-Constrain | | 5.4 |

**Figure 44: Parametric Expressions**

# Appendix B: Design explorer

The Design explorer process includes several steps before arriving at a set of optimal design solutions as shown on Figure *45*, however, the purpose of this particular study is to conduct a “what-if” study, DOE for optimum design.

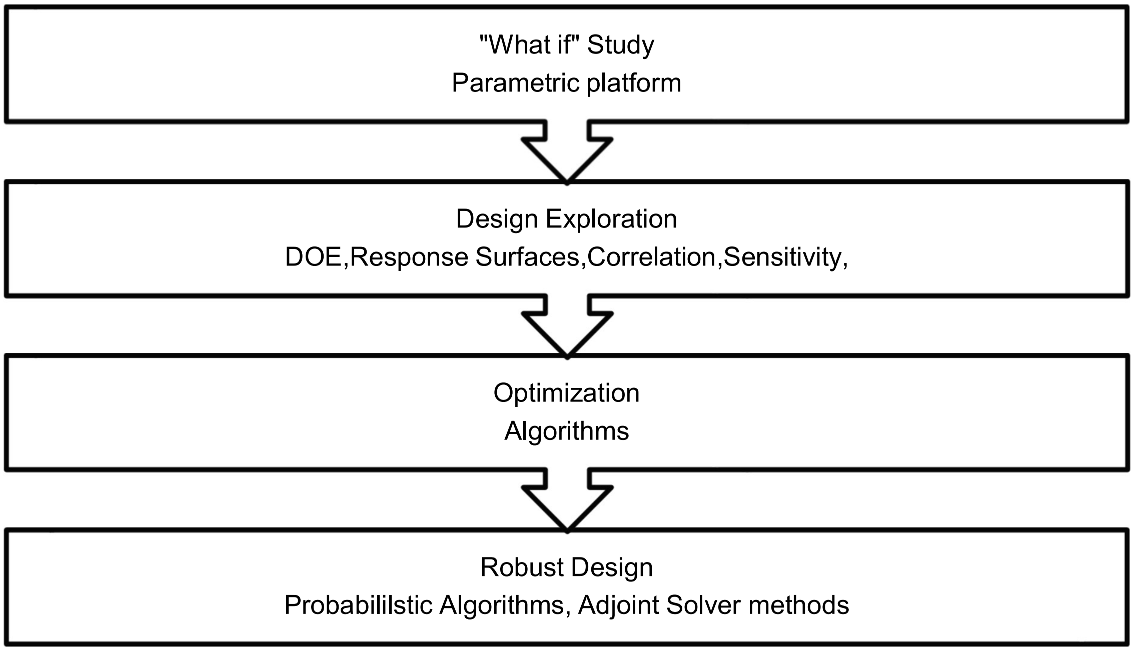

**Figure 45: Robust design steps [48]**

In a ‘’what if’’ study, the user adjusts inputs in an automated approach to decide which points to solve, this is a goal driven optimisation method and is normally set to provide guidance in objectives and constraints. The DOE scheme used for this project is Central Composite Design (CCD). CCD DOE provides a screening set to determine the overall trends of meta-model to better the choice of optimum space-filling. CCD DOE can also support up to a maximum of 20 input parameters.

The properties of CCD DOE type are indicated below and also illustrated in Figure *46*:

1. Face centered: 3 levels, not rotatable. Benefits are that it gets sampling at its extreme.
2. Rotatable 5 levels and rotatable. Drawback is it does not get sampling to extreme points.
3. VIF (Variance inflation Factor) only maximize the orthogonality

4. G-optimality: Minimize the leverage

5. Auto defined: Automatically alternates between G-optimal and VIF optimal

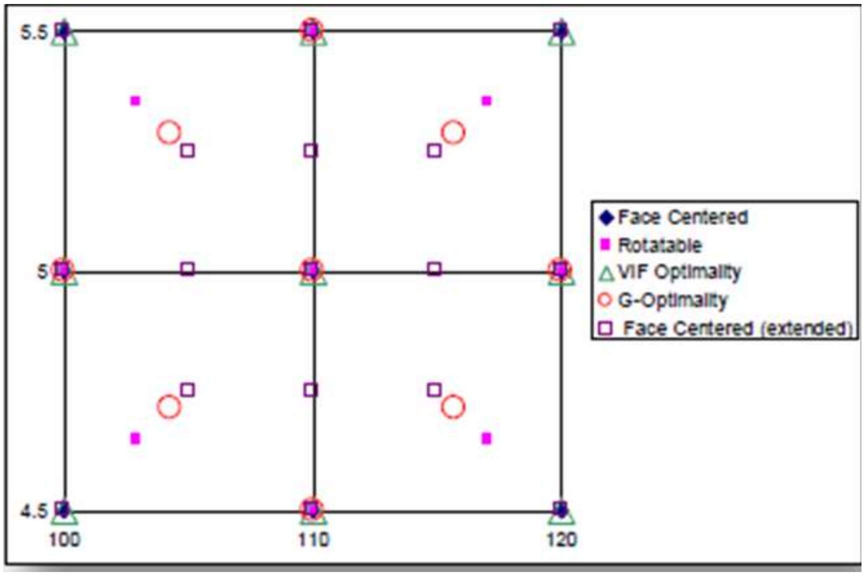

**Figure 46 : CCD DOE properties** *[48]*

**Table 16: Advantages and Disadvantage of DOE types**

| DOE algorithms types | Advantages | Dis-advantages |
|---|---|---|
| CCD | • It provides screening set to determine the overall trends of the meta-model to better guide the choice in OSF.<br>• Few design points are created but many refinery points are automatically generated with response surface,<br>• Five-level fractional factorial designs that is suitable for calibrating the quadratic response model. | • Can support a maximum of 20 input parameters. |
| OSF, | • OSF is a Latin Hypercube Sampling Design (LHS) that is extended with post-processing<br>• The Optimal Space-Filling (OSF) | |

| | | |
|---|---|---|
| | design can distribute the design parameters equally throughout the design space to gain the maximum insight into the design with the fewest number of points. | |
| BoxBehnken Design | • three-level quadratic design that does not contain fractional factorial design,<br>• requires fewer design points than a full factorial CCD and generally requires fewer design points than a fractional factorial CCD, | • Prediction at the corners of the design space is poor and that there are only three levels per parameter,<br>• A maximum of 12 input parameters is supported |
| Custom | • Allows for definition of a custom DOE Table | • Manually add new design points, entering the input and output parameter values directly into the table, |
| Custom + sampling | • Provides the same capabilities as the Custom DOE type and allows you to complete the DOE table automatically to fill the design space efficiently | |
| Sparse Grid initialization | • It refines only in the directions necessary, so that fewer design points are needed for the same quality response surface,<br>• Effective at handling discontinuities | |
| LHS | • LHS design, no point shares a row or column of the design space with any other point’<br>• Very useful when the computation time available is limited, | • LHS design are that extremes (i.e., the corners of the design space) are not necessarily covered and that the selection of too few design points can result in a lower quality of response prediction,<br>• Selecting few design points can results in low quality response. |